UNIVERSITY OF CALIFORNIA SAN DIEGO

Theoretical Modeling and Experimental Validation of Physiologically Relevant Flows and Their Applications

A dissertation submitted in partial satisfaction of the

requirements for the degree

Doctor of Philosophy

in

Engineering Sciences (Mechanical Engineering)

by

Obed A. Campos

Committee in charge:

Professor Geno Pawlak, Co-Chair
Professor Antonio L. Sanchez, Co-Chair
Professor Stephanie E. Lindsey
Professor Mitsue Miyazaki
Professor David Saintillan

2026

This dissertation of Obed A. Campos is approved, and it is acceptable in quality and form for publication on microfilm and electronically.

University of California San Diego

2026

DEDICATION

Dedicated to Jose A. Campos and Juan C. Lasheras, may their light always guide me.

TABLE OF CONTENTS

LIST OF FIGURES

LIST OF TABLES

ACKNOWLEDGMENTS

I would first like to acknowledge my family, who have been the pillars of support throughout this five-year journey. My mother and sister, Esther I. Campos and Eva R. Campos, have been guiding lights who showed me the way when times grew dark. Their strength and radiance gave me the hope I needed to keep moving forward. Alongside them, my brother-in-law, Mario I. Flores, has been a great mentor and friend, while my cousin, Sammuel E. Alafro, has been a steadfast friend and ally in times of need. My nephew, Angel A. Flores Campos, a recent addition to our family, has brought me renewed hope for the future and excitement for all that is yet to blossom. Overall, this five-year journey would not have been possible without my family.

Secondly, I would like to acknowledge my father, Jose A. Campos, who passed away before I began this five-year journey. He was an orphan from a third-world country who gave everything throughout his life to provide for me and my family and to ensure a better future for us. Truly, without him, I would not have been in the right place at the right time to meet the people who set me on this path.

One of those people was Professor Juan C. Lasheras, a mentor and father figure, who also passed away before this five-year journey began. He gave me the freedom to let my imagination run wild while fostering my growth in the field of biomechanics.

To the mentors who took over after Juan's passing, I would like to acknowledge my advisors, Professor Antonio L. Sanchez and Professor Geno Pawlak. Antonio has been my central mentor in theoretical work, making endless hours of mathematics feel engaging and exciting. Geno has been my central mentor in experimental work, helping bring to life ideas that at times seemed impossible. Together, they have shaped me into the researcher I am today.

I would also like to thank my committee members, Stephanie E. Lindsey, Mitsue Miyazaki, and David Saintillan, who have been mentors and valued colleagues throughout the years.

Next, I would like to acknowledge my friends and colleagues from Latine-Scholar Network, Ceviche Hour, Raza Centro, Pawlak Lab (Environmental Fluid Dynamics Lab), and Sanchez Lab (Multiscale Flow Physics).

Finally, I would like to thank my friends who have been part of my life over the years: Brandon Gonzalez, Genesis Discua, Don Turner, Stephanie Sincomb, Troy Sincomb, Brooklyn Asai, Richard Lint, Daibo Zhang, Guillermo L. Nozaleda, Brandon Li, Hannah Walker, Hsin-Yi Chen, Pallav Ranjan, Alex Porier, Javeir Alaminos, Aditya Potnis, Emily Beckman, Amy Schwartz, Laura Uribe, and Tanumoy Dhar.

Chapter 2, in full, is a reprint of the material as it appears in Campos, O., Alaminos-Quesada, J., Sincomb, S., Malis, V., Miyazaki, M., Coenen, W., Gutiérrez-Montes, C., Martínez-Bazán, C., Pawlak, G., & Sánchez, A. L. (2026). Phantom-Based Evaluation of Time-SLIP MRI for Measuring Spinal-Canal Lagrangian Drift.*(submitted to Scientific Reports)*.The dissertation author was the primary investigator and author of this paper.

Chapter 3, in full, is a reprint of the material as it appears in Campos, O. A., Garcia-Herreros, A., Sánchez, A. L., Fineman, J. R., & Pawlak, G. (2024). A Multichamber Pulsating-Flow Device With Optimized Spatial Shear Stress and Pressure for Endothelial Cell Testing. *Journal of Biomechanical Engineering*, *147*.The dissertation author was the primary investigator and author of this paper.

Vita

EDUCATION

2020 Bachelor of Science in Mechanical Engineering with Specialization in Controls and Robotics, University of California San Diego

2023 Master of Science in Engineering Sciences (Mechanical Engineering), University of California San Diego

2026 Doctor of Philosophy in Engineering Sciences (Mechanical Engineering), University of California San Diego

PUBLICATIONS

Campos, O., Alaminos-Quesada, J., Sincomb, S., Malis, V., Miyazaki, M., Coenen, W., Gutiérrez-Montes, C., Martínez-Bazán, C., Pawlak, G., & Sánchez, A. L. (2026). Phantom-Based Evaluation of Time-SLIP MRI for Measuring Spinal-Canal Lagrangian Drift.*(submitted to Scientific Reports)*.

Campos, O. A., Garcia-Herreros, A., Sánchez, A. L., Fineman, J. R., & Pawlak, G. (2024). A Multichamber Pulsating-Flow Device With Optimized Spatial Shear Stress and Pressure for Endothelial Cell Testing. *Journal of Biomechanical Engineering*, *147*. https://doi.org/10.1115/1.4066800

Sincomb, S., Moral-Pulido, F., Campos, O., Martínez-Bazán, C., Haughton, V., & Sánchez, A. L. (2024). An in vitro experimental investigation of oscillatory flow in the cerebral aqueduct. *European Journal of Mechanics - B/Fluids*, *105*, 180–191. https://doi.org/10.1016/j.euromechflu.2024.01.010

Schwartz, A. B., Campos, O. A., Criado-Hidalgo, E., Chien, S., del Álamo, J. C., Lasheras, J. C., & Yeh, Y.-T. (2021). Elucidating the Biomechanics of Leukocyte Transendothelial Migration by Quantitative Imaging. *Frontiers in Cell and Developmental Biology*, *9*. https://doi.org/10.3389/fcell.2021.635263

FIELDS OF STUDY

Major Field: Engineering Sciences (Mechanical Engineering)

Studies in Fluid Mechanics and Biomechanics

ABSTRACT OF THE DISSERTATION

Theoretical Modeling and Experimental Validation of Physiologically Relevant Flows and Their Applications

by

Obed A. Campos

Doctor of Philosophy in Engineering Sciences (Mechanical Engineering)

University of California San Diego, 2026

Professor Geno Pawlak, Co-Chair

Professor Antonio L. Sanchez, Co-Chair

Understanding physiological flows is essential to the advancement of medical science. This dissertation investigates two physiologically relevant flow problems and their applications through a combination of theoretical modeling and experimental analysis. The first investigation concerns cerebrospinal-fluid flow in the central nervous system, with particular emphasis on the *in vitro* experimental characterization of the slow fluid-particle drift induced by cardiac-driven motion in the spinal canal. The study shows that Time-Spatial Labeling Inversion Pulse (Time-SLIP), a non-contrast MRI technique, can be used to measure mean Lagrangian drift in a simplified phantom. It also identifies potential limitations associated with signal quality, spatial resolution, and post-processing methodology, which may complicate future clinical applications of the method. The second topic concerns blood flow in the main pulmonary artery. This problem is first addressed through the development of an *in vitro* experimental platform that applies pressure and shear

stress simultaneously to endothelial cells. The results demonstrate a working platform capable of accurately reproducing flow-induced mechanical loads over a sufficient endothelial cell population for qRNA sequencing. Complementing this experimental work, the dissertation also presents a theoretical and experimental analysis of Poiseuille flow over a stretching bottom boundary, providing the foundation for a future device capable of reproducing the full range of flow-induced mechanical loads acting on endothelial cells, including shear stress, pressure, and stretching. Experimental observations further show qualitative agreement with the theoretical predictions, supporting the use of this analysis in the development of a future device.

Chapter 1

Overview and Motivation

Understanding physiological flows is important for basic medical advancement and clinical applications. These flows dictate transport, mixing, and mechanical signaling, influencing both healthy function and disease progression. However, they remain difficult to study due to measurement limitations and the challenge of reproducing complex *in vivo* conditions in the laboratory. Addressing these challenges requires the integration of engineering principles with medical science. This dissertation contributes to that effort through the investigation of two distinct physiological-flow problems, addressed separately below.

Part I investigates cerebrospinal-fluid (CSF) flow in the spinal canal, where fluid particles undergo oscillatory motion driven by the cardiac and respiratory cycles. This motion includes a mean Lagrangian drift, representing the cumulative net displacement experienced by the fluid over each oscillatory cycle. Quantifying this motion *in vivo* is challenging because the associated velocities ($\sim$ cm min^{-1}) are much smaller than those of the dominant oscillatory flow ($\sim$ cm s^{-1}), limiting the applicability of conventional phase-contrast (PC) MRI. In **Chapter 2** we assess the suitability of Time-Spatial Labeling Inversion Pulse MRI (Time-SLIP) for characterizing this motion using in vitro experiments in a spinal-canal phantom. The phantom consists of a flexible tube with a rigid insert forming an eccentric annular canal representative of the spinal subarachnoid space, driven by a 1 Hz sinusoidal flow mimicking cardiac-induced CSF pulsations. Oscillatory velocities were measured with PC-MRI, while net fluid displacement over successive cycles was quantified using Time-SLIP and compared with direct numerical simulations. The measurements reveal spatially varying Lagrangian drift directed caudally in narrow regions and cranially in wider regions of the annulus, with magnitude scaling with the square of the local stroke volume. These

results demonstrate that Time-SLIP can quantify mean Lagrangian motion associated with pulsatile CSF flow.

Part II focuses on the design and experimental characterization of platforms to study endothelial-cell responses under similar conditions as in the main pulmonary artery. In vascular pathologies like pulmonary hypertension, endothelial cells experience coupled hemodynamic loads: wall shear stress, pulsatile pressure, and wall stretching. Reproducing these conditions *in vitro* is essential for disease-focused mechanobiological studies that can help devlop pharmacetiucals in the future. **Chapter 3** establishes the fluid-mechanical framework for an apparatus that generates a constant shear stress at different pressure ranges across multiple series-connected chambers. By combining theoretical, numerical, and experimental analyses, this chapter characterizes the device's pulsatile flow, pressure, and shear-stress environments, providing a validated platform for future studies of endothelial-cell behavior under complex vascular conditions. **Chapter 4** extends the previous work by developing the theoretical framework required to design a device capable of accurately applying all three mechanical loads to endothelial cells. This framework is subsequently validated through experimental analysis, with qualitative results showing good agreement with the theoretical predictions.

Part I

Cerebrospinal Fluid Transport and Noninvasive Flow Quantification

Chapter 2

Phantom-Based Evaluation of Time-SLIP MRI for Measuring Spinal-Canal Lagrangian Drift

2.1 Introduction

The cerebrospinal fluid (CSF) that fills the cerebral ventricles and the subarachnoid space (SAS) surrounding the brain and spinal cord undergoes cyclic motion synchronized with the cardiac and respiratory cycles. In the spinal canal, this oscillatory flow reaches peak velocities on the order of a few centimeters per second [1, 2]. Although the flow is largely oscillatory, fluid parcels do not return exactly to their original positions at the end of each cycle. This results in a slow net displacement—referred to as Lagrangian drift—superimposed on the fast, periodic motion [3–5].

While the stroke length of the oscillatory motion in the spinal canal is typically on the order of one centimeter [1, 2], the net particle displacement per cycle is much smaller—only a fraction of a millimeter—corresponding to mean Lagrangian velocities of a few centimeters per minute [5, 6]. Being a closed domain, the mean Lagrangian flow inside the spinal canal must have zero net volumetric flux, implying the coexistence of simultaneous caudal and cephalic flow components across any transverse section. This bidirectional behavior, first observed by Di Chiro using radioactive tracers [7], is believed to play an important role in the transport of nutrients and metabolic waste, as well as in the dispersion of drugs administered intrathecally in the lumbar region [4, 6].

There is considerable interest in noninvasively characterizing oscillatory CSF motion, given its relevance to several central nervous system disorders, including normal pressure hydrocephalus and syringomyelia. A widely used imaging modality is phase-contrast magnetic resonance imaging

(PC MRI), which encodes fluid velocity into the phase of the MR signal, enabling time-resolved measurements of the Eulerian velocity field [8]. PC MRI has been successfully applied to capture CSF motion driven by cardiac [9] and respiratory [10] cycles in the spinal SAS, as well as in the cerebral ventricles and their connecting foramina [11, 12].

Although PC MRI provides valuable information about oscillatory flow, it lacks the sensitivity needed to resolve the small velocities associated with mean Lagrangian drift [13]. Accurately capturing this slow motion requires the use of invasive tracer-based techniques capable of tracking the actual movement of fluid elements, that being the approach taken by Di Chiro [7] and others (see, e.g. [14]). The starting point of the current analysis is the realization that non-invasive imaging methods based on magnetic resonance spin labeling may be well suited for tracking the Lagrangian motion of the fluid. In particular, we will be using Time-Spatial Labeling Inversion Pulse (Time-SLIP) MRI, a non-contrast technique developed to view and assess fluid displacement [15]. The technique works by first applying a nonselective inversion pulse to invert the entire magnetization, followed by a selective pulse that restores magnetization within a designated region, effectively creating a "tagged" volume of fluid. This tagged region can be tracked, enabling visualization of the underlying Lagrangian motion over subsequent oscillatory cycles. The duration of the time window during which the tagged fluid can be visualized, usually a few seconds, is governed by the relaxation time of the fluid [16].

The development of Time-SLIP MRI as a tool to quantify CSF flow is due to Yamada et al. [17], who built on earlier arterial spin-labeling techniques proposed in the 1980s for studying blood flow and perfusion [18–22]. Time-SLIP has since been employed to characterize, for example, the effects of respiration on intracranial CSF motion [23], pathologic CSF flow in the spinal cord [24, 25], cervical flow in patients with Chiari Type I malformation [26], and CSF dynamics in the mid-cervical and craniocervical junction regions of adolescents with idiopathic scoliosis [27]. Reviews summarizing the respective strengths of PC and Time-SLIP MRI for diagnosing and managing CSF flow disorders are available in the literature [13, 28]. Phantom studies have also been employed to test the predictive capabilities of Time-SLIP in connection with the characterization of

different flows. For instance, water phantoms have been employed in Time-SLIP studies of general slow and complex fluid flows [29], CSF flow around Liliequist membranes and arachnoid-cyst walls [30], pulsatile flow in pipes of variable section [31], salivary flow in the parotid duct [32], and slow pancreatic juice flow [33].

Like these previous studies, this paper employs a flow phantom to investigate the capabilities of Time-SLIP MRI in quantifying the mean Lagrangian displacement of cerebrospinal fluid (CSF) driven by cardiac motion in the spinal canal. It is hypothesized that the available measurement window—a few seconds following pulse labeling—is sufficient to capture the Lagrangian displacement of CSF fluid over several cardiac cycles. To test this hypothesis, we designed and built a simplified model of the spinal canal consisting of an eccentric, compliant annular space sealed at one end. The phantom is tested in a 3 T Siemens MRI scanner, using phase-contrast (PC) MRI to characterize the oscillatory flow and Time-Spatial Labeling Inversion Pulse (Time-SLIP) MRI to capture the associated cyclic Lagrangian drift. The measurements are compared with MRI-informed direct numerical simulations based on the Navier–Stokes equations. Semi-automatic image processing is employed to quantify the cyclic Lagrangian displacements. Analysis of the signal-to-noise ratio provides insight into the limitations of the technique with respect to spatial resolution, as well as its dependence on stroke volume and number of cycles. The results, which highlight both the potential and the limitations of Time-SLIP for characterizing Lagrangian drift, lay the groundwork for future *in vitro* investigations.

2.2 Methods

2.2.1 Spinal Canal Phantom: Design and Experimental setup

The spinal SAS is a compliant annular channel of length $L \sim 40$–60 cm and characteristic width $h \sim 4$ mm, bounded internally by the pia mater surrounding the spinal cord and externally by the deformable dura membrane. As shown in Fig. 2.1a, the canal is eccentric: the spinal cord lies closer to the posterior side of the dura in the cervical and lumbar regions, and closer to the

anterior side in the thoracic region. This eccentricity has been shown to play an important role in the resulting CSF motion [5].

The CSF filling the canal undergoes pulsatile motion driven by periodic pressure variations induced by the cardiac and respiratory cycles. These fluctuations are accommodated by venous blood displacement and compression of the fatty tissue in the epidural space surrounding the dural sac. The dominant oscillatory flow, characterized by stroke lengths $L_s \sim 1$ cm and a nearly zero net flow rate, is spatially non-uniform, promoting nonlinear interactions that give rise to a persistent bidirectional secondary flow that recirculates fluid along the canal.

The phantom, shown in Fig. 2.1b, is designed to maximize simplicity while retaining the key features of the spinal SAS, namely an eccentric annular geometry with a closed end and a deformable outer boundary. The spinal cord is represented by a rigid rod insert of radius $R_i = 5$ mm, while the dura membrane is modeled by a coaxial flexible tube (silicone, Ecoflex OO-30) of radius $R_o = 11$ mm and length $L = 28$ cm. To facilitate flow measurements, the flexible tube is connected upstream to a rigid transparent tube with the same inner radius $R_o = 11$ mm, providing a non-deformable annular section. As indicated in the inset near the bottom of Fig. 2.1b, the eccentricity is imposed by offsetting the longitudinal axes of the tube and rod by a distance $\beta(R_o - R_i)$, which is kept constant along both the flexible and rigid sections of the phantom. The entire setup is placed inside a custom container that allows the flexible section to rest on a platform, mimicking a subject lying supine in an MRI scanner, as shown in Fig. 2.1c.

To mimic cardiac-driven flow, a programmable piston pump (SuperPump AR, ViVitro Labs, Victoria, Canada), located outside the MRI room, was connected via tubing of corrugated PVC to the rigid stretch of the phantom. Water was used as the working fluid because its density $\rho \simeq 10^3$ kg/m^3, kinematic viscosity $\nu \simeq 0.7\times10^{-6}$ m^2/s, and magnetization properties are similar to those of CSF. For simplicity, the experiments employed the sinusoidal flow rate $Q_0(t) = \mathcal{Q}\sin(\omega t)$ shown in Fig. 2.1d, with peak amplitude $\mathcal{Q}$ and angular frequency $\omega = 2\pi$ s^{-1} (60 beats per minute), corresponding to a cardiac period $T = 2\pi/\omega = 1$ s. The associated Womersley number, $\alpha = [\omega(R_o - R_i)^2/\nu]^{1/2} \simeq 18$, is comparable to, although somewhat larger than, that characterizing

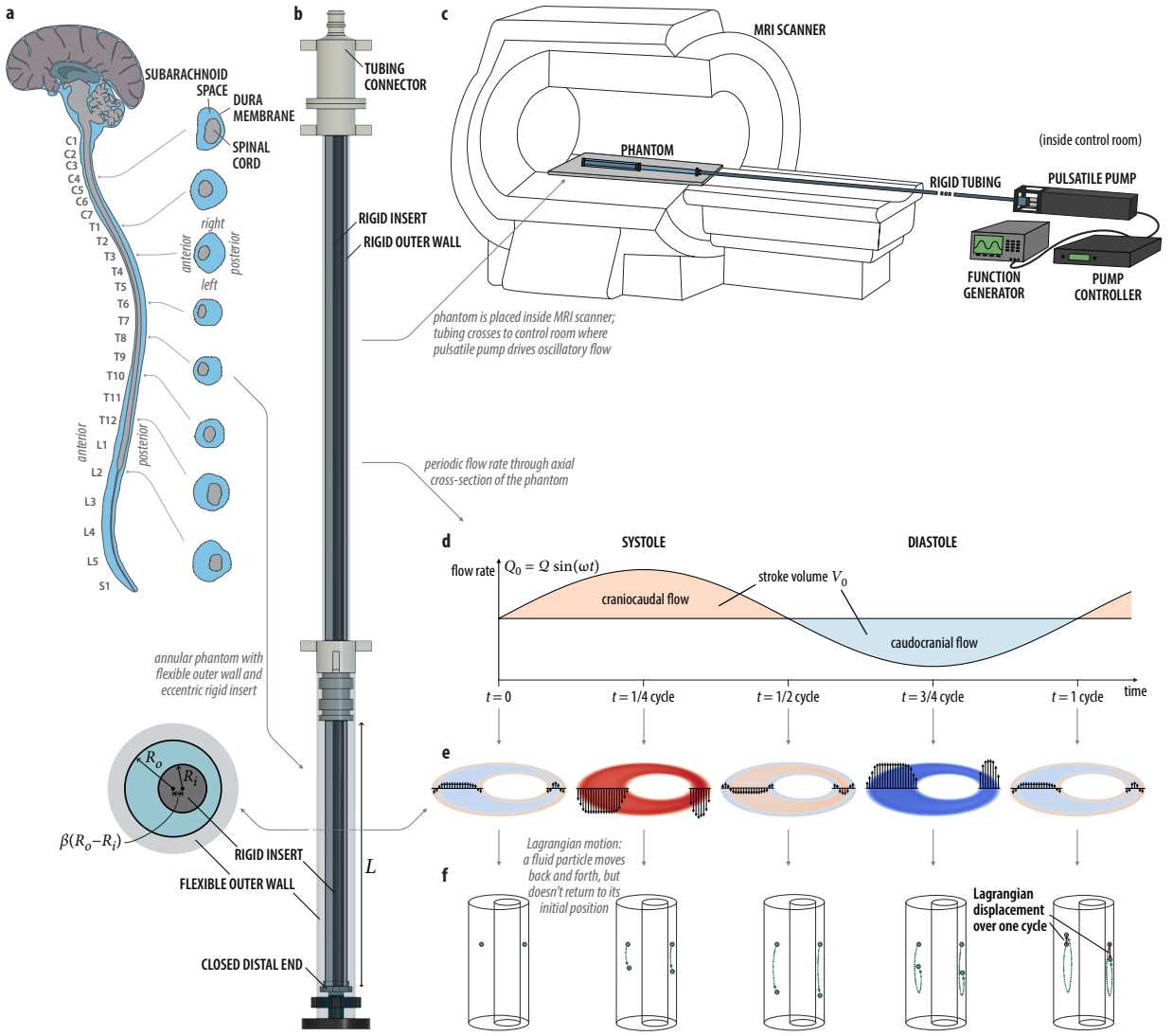

Figure 2.1: **(a)** Schematic diagram of the human subarachnoid space, showing the eccentric location of the spinal cord within the spinal canal. **(b)** Spinal canal phantom, with indication of its rigid and flexible parts, and the eccentric placement of the insert that mimics the spinal cord. **(c)** The phantom is placed inside the MRI scanner and is connected via rigid tubing to a pulsatile pump inside the control room. **(d)** The pulsatile pump drives a periodic flow rate through the phantom. **(e)** Snapshots of the (Eulerian) velocity distribution at different phases of the oscillation cycle. **(f)** Schematic illustrating how, in every cycle, fluid moves back and forth, but does not return to its initial position, resulting in a net Lagrangian displacement.

flow in the human spinal SAS ($\alpha \simeq 12$). As shown in [3], such differences in Womersley number do not lead to significant qualitative changes in the resulting mean Lagrangian motion.

The local flow rate Q, equal to Q_0 in the rigid section of the canal, decreases with distance from the entrance of the flexible tube x and vanishes at the closed end of the canal ($x = L$). Correspondingly, the stroke volume $V_s(x) = \frac{1}{2}\int_t^{t+T} |Q|\,\mathrm{d}t$ and the associated stroke length $L_s(x) = V_s(x)/[\pi(R_o^2 - R_i^2)]$ also decrease from their entrance values $V_s(0) = V_0 = \frac{1}{2}\int_t^{t+T} |Q_0|\,\mathrm{d}t = 2Q/\omega$ and $L_s(0) = L_0 = V_0/[\pi(R_o^2 - R_i^2)]$ to zero at $x = L$. Because the tubing connecting the pump to the phantom is not fully rigid, small—yet non-negligible—spatial variations of the flow rate can be expected to occur along the feed line, so that the stroke volume at the phantom entrance, $V_0 = V_s(0)$, can differ from the pump output. Consequently, separate provisions were made to measure V_0, as described below.

2.2.2 Phase Contrast MR: Acquisition and Analysis

MR imaging was performed at the Mind, Brain, and Behavior Research Center of the University of Granada on a 3T Magnetom Prisma Fit scanner (Siemens Healthineers, Forchheim, Germany) using a 32-channel spine coil (`https://cimcyc.ugr.es/en/research/equipment/rmf`). A 2D PC MRI sequence with the section orientation perpendicular to the lengthwise axis of the phantom was applied to acquire the fluid velocity data at different transverse sections $x = (7, 14, 21)$ cm along the flexible part of the phantom, corresponding to dimensionless distances $x/L = (0.25, 0.5, 0.75)$. To accurately evaluate the entrance stroke volume V_0, additional measurements were acquired in the rigid tube at a location 15 cm upstream from the phantom entrance. The PC MRI parameters included the following: flip angle=10°, field of view=160×160 mm^2, matrix=256×205, in-plane resolution=0.625×0.78 mm^2 reconstructed to 0.625×0.625 mm^2, section thickness=10 mm.

For each value of the pump stroke volume and location, the velocity encoding was adjusted to the anticipated optimum, with echo times and repetition times varying correspondingly between 6.38 and 7.2 ms and 21.06 and 94.38 ms, respectively. The piston position of the pulsatile pump

was used as an external signal for the retrospective gating of the PC MR protocol. Each acquisition yielded 40 phases per cycle. The PC MR images were processed using custom MATLAB code to obtain the 2D distribution of longitudinal fluid velocity at each measured cross-section of the phantom for each phase. Owing to the canal eccentricity, the resulting oscillatory velocity field exhibits strong azimuthal non-uniformity, as schematically illustrated in Fig. 2.1e. The velocity fields were then numerically integrated over the cross-sectional area to obtain the flow rate $Q(x,t)$ through each section as a function of time t. Finally, integration of the flow rate over a complete oscillatory cycle yielded the stroke volume variation $V_s(x) = \frac{1}{2}\int_0^T |Q(x,t)|\,\mathrm{d}t$.

2.2.3 Time-SLIP: Acquisition and Analysis

As explained in previous analyses [3, 4, 6, 34], the spatial non-uniformity of the oscillatory velocity field implies that, at the end of each motion cycle, individual fluid particles do not return to their exact initial locations but instead experience a small net displacement, as schematically illustrated in Fig. 2.1f. The accumulation of these small displacements over subsequent cycles produces the net bulk motion first observed by Di Chiro [7].

To measure the net cyclic displacement in our phantom, two-dimensional Time-SLIP images were acquired using a balanced steady-state free-precession sequence (native TrueFISP, Siemens), applied to a transverse band spanning 10 mm in the longitudinal direction. The contrast mechanism underlying this sequence is illustrated in Fig. 2.2a and relies on signal preparation within the imaging section at $t = 0$, followed by an image readout after a time $t = \mathrm{TI}$ (known as the "inversion time"). First, a nonselective inversion pulse is applied to the entire imaging volume, immediately followed by a spatially selective inversion pulse applied only to a 10 mm $\times$ 10 mm-thick rectangular prism whose long axis is aligned with the symmetry plane of the phantom and is perpendicular to the cylinder axis. As a result, the magnetization within this region is tipped back to its original value and thereafter remains constant (commonly referred to as the "labeled" volume), while the surrounding inverted background recovers exponentially with relaxation time T_1. Upon image readout after a time $t = \mathrm{TI}$, the labeled volume consistently shows up bright, whereas the background image

intensity depends on the extent to which the magnetization has been able to recover during the time TI. Because the relaxation time T_1 of water is approximately 3–4s, the resulting contrast between the labeled volume and the background, which occurs when the magnetization of the background crosses zero, is maximum around 2–3s (see Fig. 2.2a). After 5–6s, the labeled volume is only weakly distinguishable from the background.

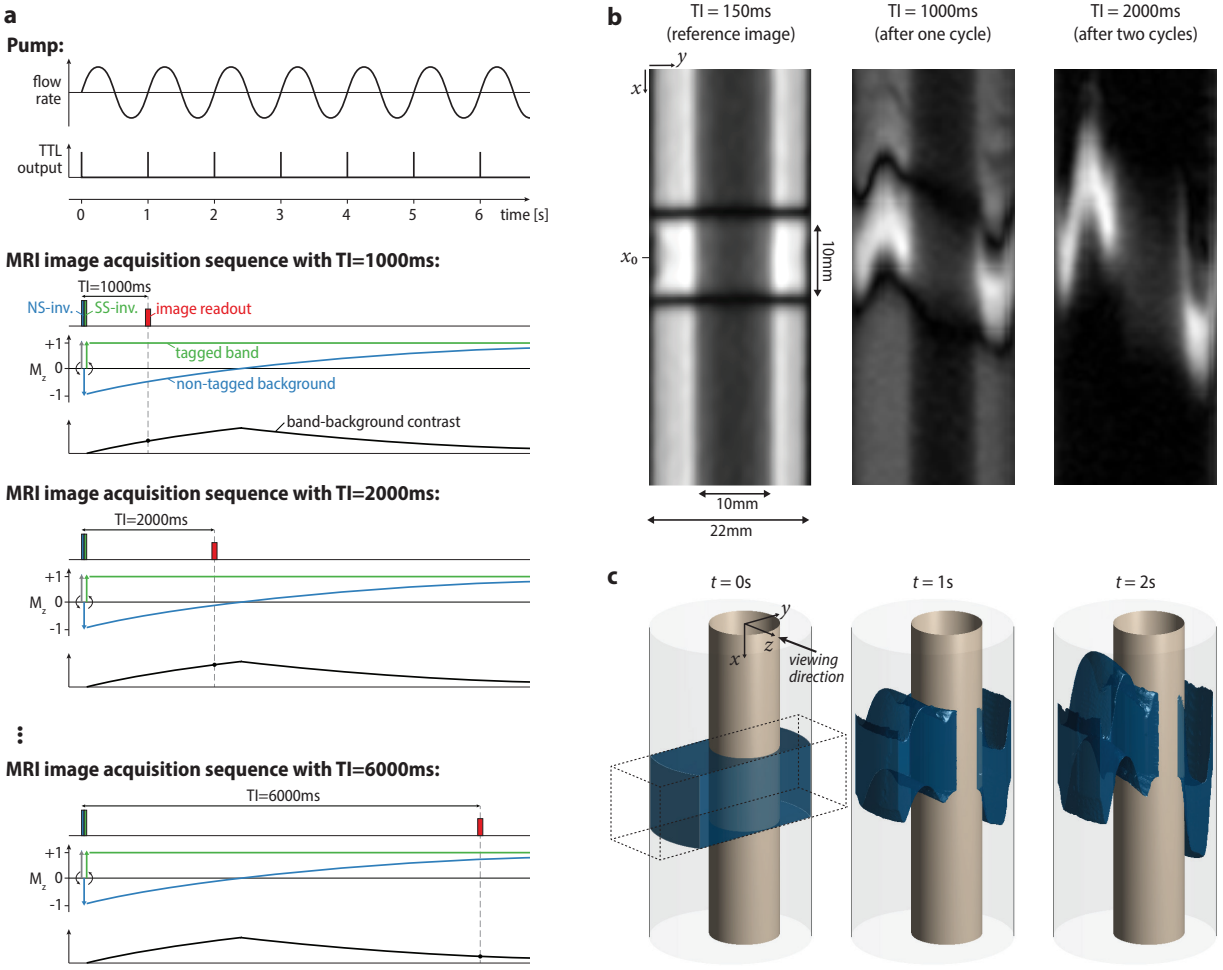

Figure 2.2: **(a)** Time-SLIP MR sequence synchronized with the pulsatile pump, using TI equal to 1 up to 6 complete oscillation cycles. **(b)** Time-SLIP yields 2D images that show the net Lagrangian displacement of a band of tagged fluid over one or more oscillation cycles. **(c)** 3D direct numerical simulation replicates the Lagrangian motion of the tagged fluid region.

To quantify the net cyclic displacement of the fluid, i.e. the displacement over a number n of complete oscillation cycles (with period $T = 1$ s), we employ inversion times equal to TI = nT. In particular, for each stroke volume and measured location along the phantom, we performed six

acquisitions, using TI = 1000 ms, 2000 ms, . . . , 6000 ms. The position x_0 of the labeled volume at $t = 0$ was determined from a reference image taken in the absence of fluid motion. Note that the Time-SLIP sequence was synchronized with the programmable pump using its TTL output, such that $t = 0$ corresponds to zero flow rate in the phantom (top panel of Fig. 2.2a). Figure 2.2c shows the initial location of the tagged fluid, and after one and two oscillation periods, reflecting the cumulative net Lagrangian displacement.

The image acquisition plane of the Time-SLIP technique is set along the symmetry plane of the phantom. The technique outputs a two-dimensional image corresponding to an average over the viewing direction perpendicular to this plane, with image brightness being proportional to the volume of tagged fluid across the section (Fig. 2.2b). As a result, the Time-SLIP images exhibit a distinct band of enhanced signal intensity associated with the labeled fluid displaced during the oscillatory motion. Note that due to the annular shape of the phantom, a weak signal intensity is obtained at the location of the cylindrical insert.

To quantitatively characterize the spatial location of this band, we reduce its two-dimensional extent to a single representative curve $x_w(y)$, which describes the longitudinal position of the tagged fluid as a function of the transverse coordinate y. Each point x_w is extracted independently from the longitudinal intensity profile $I(x)$ at a given y using the following image-processing procedure, implemented in MATLAB. First, the images were cropped to the interior of the phantom (Fig. 2.3a). For each spanwise position y, the corresponding longitudinal intensity profile $I(x)$ was extracted and normalized (Fig. 2.3b). The approximate location of the labeled band—identified as a broad peak in $I(x)$—and of the background was determined using a threshold mask. A smoothing spline was then fitted to the background signal and subtracted from $I(x)$. A second threshold mask was applied to the background-subtracted profile to refine the identification of the upper and lower bounds x_a and x_b of the intensity peak (Fig. 2.3c,d). Finally, the band location x_w was computed as an intensity-weighted average, $x_w = \int_{x_a}^{x_b} I^n(x)\, x\, \mathrm{d}x / \int_{x_a}^{x_b} I^n(x)\, \mathrm{d}x$, where the exponent n controls the relative weighting of the peak intensity within the band. For the results presented here, $n = 8$ was found to provide good visual agreement between the extracted curve $x_w(y)$ and

the bright band observed in the Time-SLIP images (Fig. 2.3e). Using the same decomposition of the intensity profile into peak and background regions, we additionally define a spanwise signal-to-noise ratio $\mathrm{SNR}(y)$ to assess the reliability of the extracted displacement. The signal is quantified as the integrated intensity within the band, $S(y) = \int_{x_a}^{x_b} I(x)\,\mathrm{d}x$, while the noise level is estimated from the root-mean-square intensity fluctuations in the background region $\Omega_b = \{x \notin [x_a, x_b]\}$, $\sigma_b(y) = \left[\frac{1}{L_b}\int_{\Omega_b}\left(I(x) - \overline{I}_b\right)^2 \mathrm{d}x\right]^{1/2}$, where $\overline{I}_b(y) = \frac{1}{L_b}\int_{\Omega_b} I(x)\,\mathrm{d}x$ is the average background intensity and L_b denotes the longitudinal extent of the background region. The signal-to-noise ratio is then defined as $\mathrm{SNR}(y) = S(y)/\sigma_b(y)$. All integrals are evaluated numerically from the discretely sampled intensity profiles.

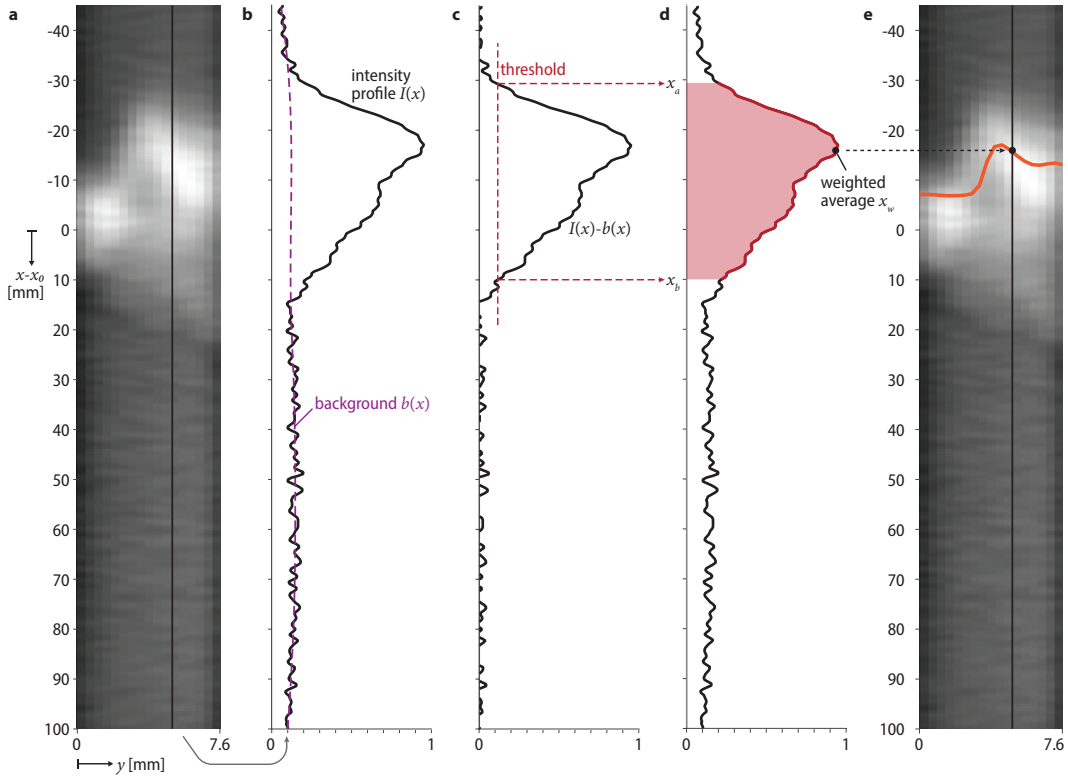

Figure 2.3: Semi-automatic image-processing procedure used to quantify the cyclic Lagrangian displacement from the Time-SLIP images. The workflow includes image thresholding, tagged-region detection, centerline extraction, and displacement estimation across successive inversion times.

2.2.4 Direct Numerical Simulation (DNS): Computations and Analysis

Three-dimensional unsteady direct numerical simulations were performed to complement the MRI measurements. The computational domain, representing the annular canal, was generated using ANSYS Fluent Meshing (2023 R1; Ansys Inc., Pennsylvania) and consisted of a structured grid comprising approximately 2×10^6 hexahedral cells. The Navier–Stokes equations for an incompressible Newtonian fluid, with density and viscosity equal to those of the water used in the experiments, were solved numerically using the finite-volume solver ANSYS Fluent (2023 R1; Ansys Inc., Pennsylvania). The numerical integration of the equations employed second-order accuracy in both space and time.

A dynamic mesh approach was employed to account for the deformation of the flexible tube [35–38], whose radius R varies periodically in time from its unperturbed value R_o as dictated by the integral continuity balance

$$\frac{\partial}{\partial t}\left(\pi R^2\right) + \frac{\partial Q}{\partial x} = 0. \tag{2.1}$$

As discussed later, the PC-MRI measurements reveal a nearly linear axial distribution of the flow rate, consistent with a spatially uniform tube radius that varies in time according to $\pi(R^2 - R_o^2) = -\int Q_0 \mathrm{d}t/L = \mathcal{Q}\cos(\omega t)/(L\omega)$, as follows from integration of (2.1), finally yielding

$$\frac{R}{R_o} = \left[1 + \frac{V_0}{2\pi R_o^2 L}\cos(\omega t)\right]^{1/2} \tag{2.2}$$

for the tube-radius variation from its unperturbed value R_o. Note that the deformation imposed is relatively small, since $V_0 \ll 2\pi R_o^2 L \simeq 212.88$ mL in all experiments and corresponding numerical computations.

Tracer particles were used to compute the mean Lagrangian displacement [6, 39]. Specifically, a cloud of massless particles, initially occupying the region corresponding to the Time-SLIP measurements (10 mm in thickness and 10 mm in axial extent), was tracked over six oscillatory cycles. The particle cloud position after each cycle provided the instantaneous location and shape

of the tagged region, as illustrated in the sample results shown in Fig. 2.2c. For comparison with the two-dimensional Time-SLIP maps, a transverse average was performed across the thickness of the region, yielding a two-dimensional image, in which the local intensity at a given $x - y$ location is linearly proportional to the number of particles found in the transverse direction (i.e. the *viewing* direction indicated in the first panel of Fig. 2.2c), analogous to the tagged fluid in the Time-SLIP MR images.

2.3 Results

2.3.1 PC Measurements

The oscillatory motion was characterized using PC MRI, with the results summarized in Fig. 2.4. Measurements were performed at several axial locations, indicated in Fig. 2.4a, for four different pump stroke volumes. The measured velocity fields were used to evaluate the local stroke volume, with the results shown in Fig. 2.4b. The stroke volume, which is constant along the rigid tube, is observed to decay linearly with the distance x from the entrance of the flexible tube. This behavior is consistent with an outer radius undergoing an axially uniform temporal variation, thereby justifying the use of Eq. (2.2) in the numerical computations.

Representative PC MRI velocity distributions measured at the midsection of the flexible tube ($x = 14$ cm) for an entrance stroke volume $V_0 = 23.5$ mL are shown in Fig. 2.4c at five equally spaced instants over the oscillatory cycle. For reference, the dashed circles denote the surface of the cylindrical inset of radius R_i and the surface of the unperturbed flexible tube of radius R_o. The images reveal a small but non-negligible variation of the cross-sectional area, with the tube adopting a slightly non-circular shape due to the influence of the resting platform.

The periodic temporal variation of the flow rate $Q(t)$, computed by integrating the velocity over the spinal-canal cross sections at $x = (7, 14)$ cm, is shown in Fig. 2.4e. Results are reported for the 40 phases sampled over one cycle. The measurements closely follow the sinusoidal variation $Q = (\omega V_0/2)(x/L)\sin(\omega t)$, with no measurable phase lag between the two locations, consistent

with the prescribed tube-radius variation given in Eq. (2.2).

The PC MRI measurements are compared with corresponding DNS results in Fig. 2.4d, obtained using the prescribed flexible-tube radius variation given by Eq. (2.2), represented by the solid-line circle. Excellent agreement is observed between the computations and the MR measurements. In both cases, the velocity profile is nearly uniform, as expected for the relatively large Womersley number $\alpha = 18$ characterizing the flow. Thin, low-velocity Stokes layers are present near both the inner and outer boundaries. The velocity distributions at $t = 0$ indicate that flow reversal first occurs within the Stokes layers adjacent to the bounding surfaces, a well-known feature of wall-bounded oscillatory flow that is consistently captured by both PC MRI measurements and DNS.

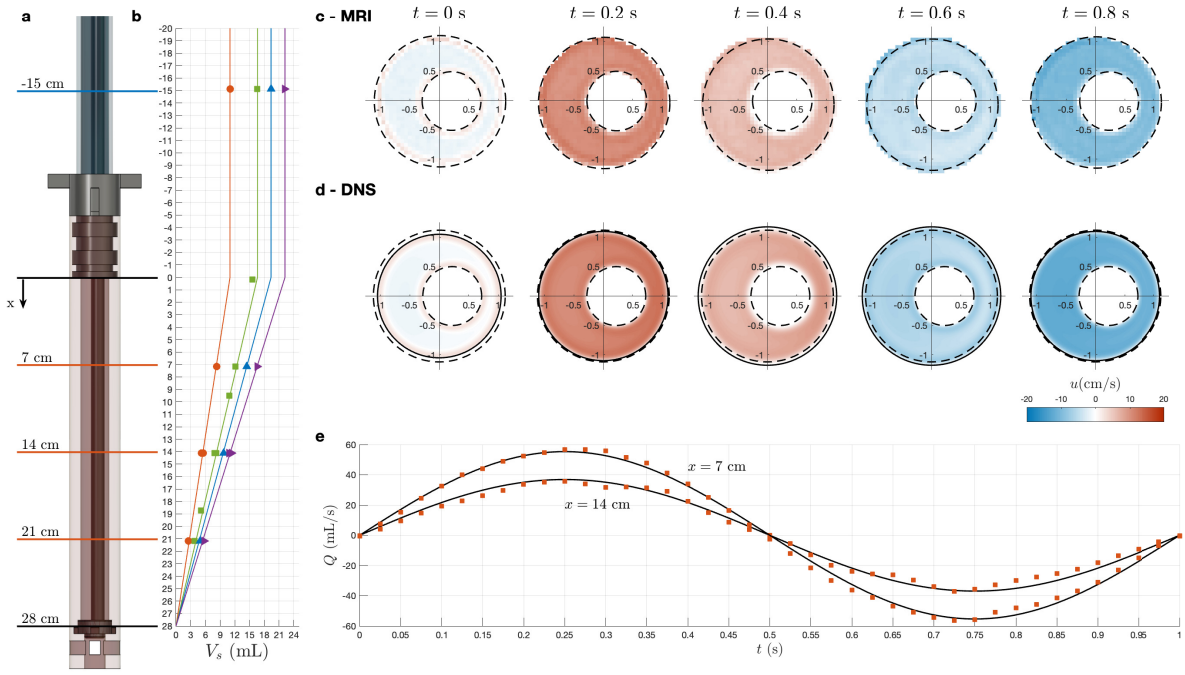

Figure 2.4: **(a)** Schematic of the phantom with an indication of the cross sections where PC MRI was taken. **(b)** Streamwise distribution of stroke volume corresponding to four different pump outputs. **(c)** PC MRI velocity measurements measured at $x = 14$ cm for $V_0 = 23.5$ mL and five different instants of time, with the dashed circles representing the surface of the inset and the surface of the unperturbed flexible tube. **(d)** DNS velocity predictions for the conditions and locations described in **(c)**, with the solid circle representing the instantaneous location of the flexible tube. **(e)** Temporal variation of the flow rate at $x = 7$ cm and $x = 14$ cm for $V_0 = 23.5$ mL (symbols) and accompanying theoretical prediction $Q = (\omega V_0/2)(x/L)\sin(\omega t)$.

2.3.2 Time-SLIP Measurements

Sample Time-SLIP images acquired at two axial locations $x_0 = (14, 21)$ cm using six different inversion times TI = 1000–6000 ms during oscillatory flow with an entrance stroke volume $V_0 = 23.5$ mL are shown in grayscale in the left-hand sides of the double panels in Fig. 2.5. The reference image of the tagged fluid at the initial time, shown in the leftmost panel, was acquired in quiescent fluid using the minimum inversion time available on the scanner (TI = 150 ms). The right-hand side of each panel shows the corresponding DNS results for the same stroke volume, with the integrated concentration of tagged fluid particles at a given location represented in blue scale.

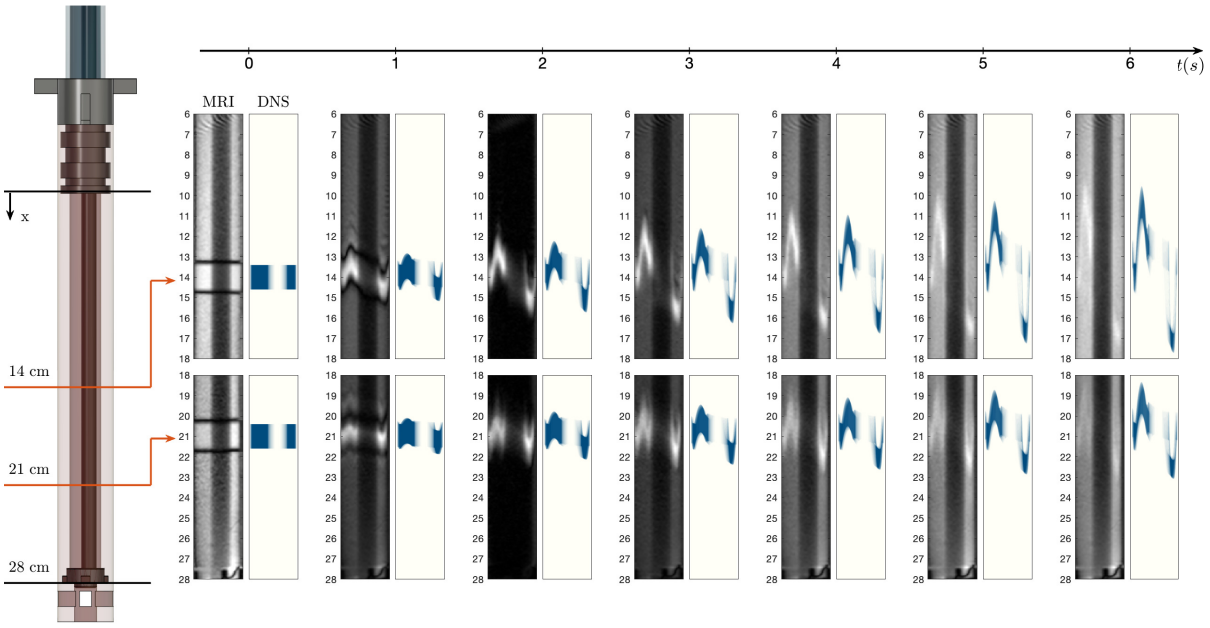

Figure 2.5: The seven double panels show Time-SLIP images acquired at different inversion times at $x_0 = (14, 21)$ cm for an entrance stroke volume $V_0 = 23.5$ mL (left, black-and-white), together with the corresponding DNS predictions of the tagged-particle distribution at the end of six successive cardiac cycles (right, color).

Figure 2.6 summarizes the Time-SLIP measurements of Lagrangian displacement for three inversion times, TI = (1000, 2000, 3000) ms—characterizing the motion over three consecutive cardiac cycles—and for entrance stroke volumes in the range $0 < V_0 < 23.5$ mL. Measurements

were obtained across the midsection of the flexible tube ($x_0 = 14$ cm), where the local stroke volume is half the entrance value, $V_s = V_0/2$. For each inversion time and each stroke volume, the panels in Fig. 2.6a show the spatial variation of the Lagrangian displacement across the canal. As in the results in Fig. 2.5, the fluid is observed to move *cranially* (i.e. toward the entrance) on the wider side of the eccentric canal and *caudally* (i.e. toward the closed end) on the narrower side.

To further characterize the Lagrangian motion, the figure also shows the dependence of the medial-axis displacement, δ_j, on each side of the canal on the local stroke volume, V_s, where the subscript j denotes the inversion time (in seconds). Dashed curves corresponding to parabolic fits are included for reference. For completeness, the displacement per cycle, δ_c, obtained by dividing δ_j by the number of cycles associated with each inversion time j, is shown in Fig. 2.6b.

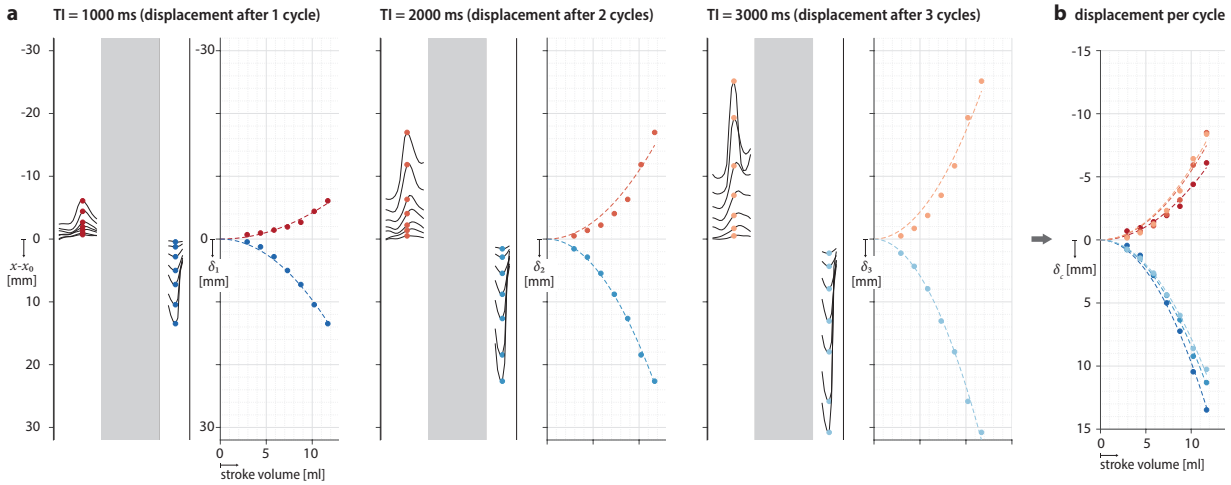

Figure 2.6: Systematic evaluation of mean Lagrangian displacement from a series of Time-SLIP measurements at $x_0 = 14$ cm for TI $= (1000, 2000, 3000)$ ms and $V_s = (2.9, 4.4, 5.8, 7.3, 8.8, 10.2, 11.7)$ mL. **(a)** Transverse profiles along with the corresponding variation with V_c of the displacement at the median axis on both sides of the canal after one (δ_1), two (δ_2), and three (δ_3) cycles. **(b)** Corresponding cyclic displacement evaluated according to $\delta_c = (\delta_1, \delta_2/2, \delta_3/3)$.

The SNR of the Time-SLIP measurements was evaluated to examine the variation in image quality with inversion time and with stroke volume. Results for the section at $x_0 = 14$ cm are presented in Fig. 2.7 for the seven stroke volumes shown in Fig. 2.6. The central panels show the spatial distribution of SNR across the spinal canal for six different inversion times, corresponding to displacements accumulated over six consecutive cardiac cycles. To examine the effects of the

walls, the transverse distribution of the SNR averaged over inversion times and stroke volumes is shown in the upper panels. Similarly, the influence of inversion time is quantified in side bar graphs showing SNR values averaged spatially across the canal and over all stroke volumes.

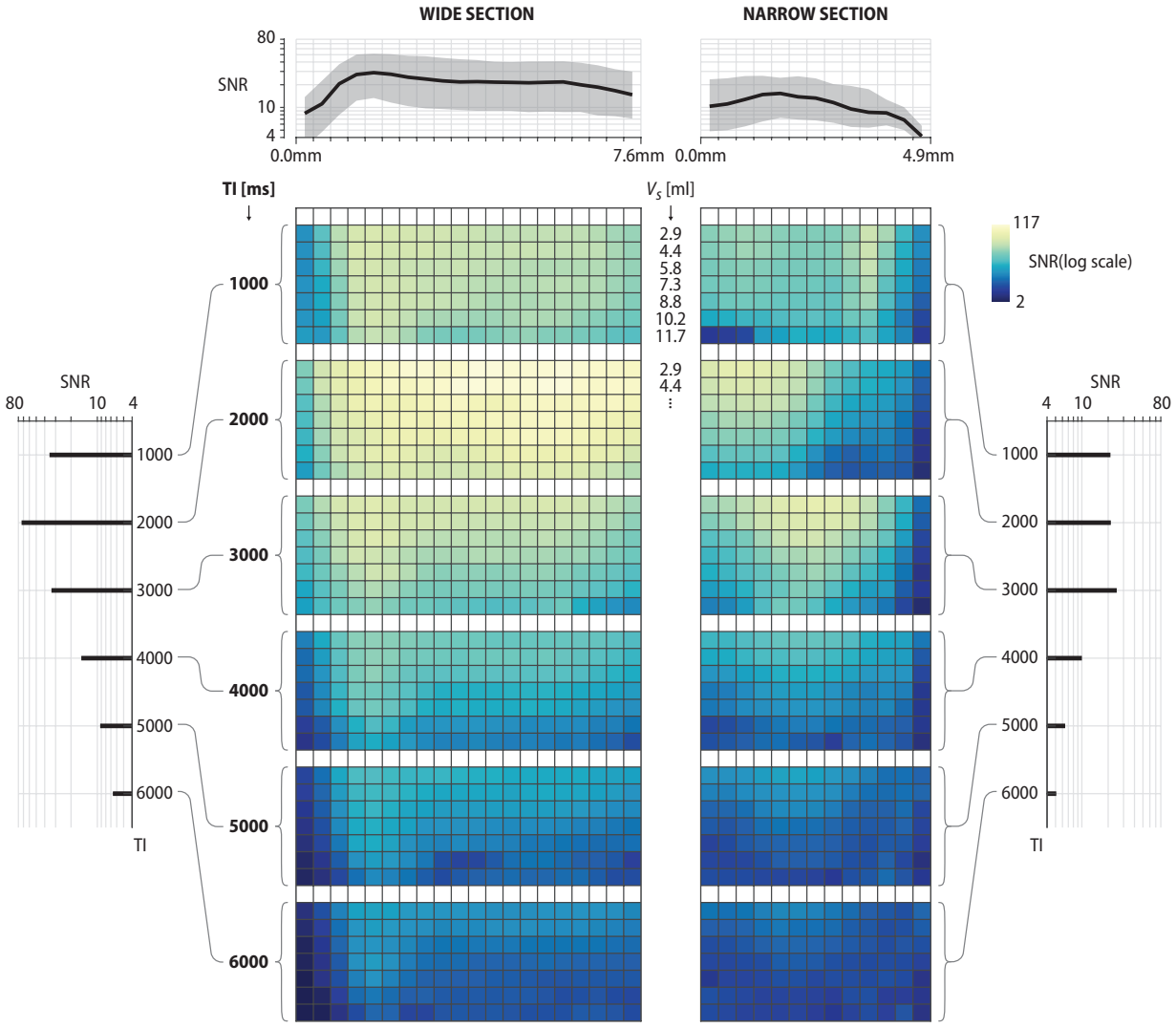

Figure 2.7: The color plots show the local signal-to-noise ratio (SNR) systematically evaluated from a series of Time-SLIP measurements at $x_0 = 14$ cm for selected values of TI and V_s. The upper panels display the transverse distribution of SNR averaged over all TI and V_s, while the side bar graphs report SNR values averaged spatially across the canal and over all stroke volumes.

2.4 Discussion

Excellent agreement between the Time-SLIP images and the corresponding DNS predictions is demonstrated in Fig. 2.5. The MR technique accurately captures the shape of the progressively distorted bolus of tagged fluid over the six cardiac cycles shown, although visual comparison becomes more challenging at higher inversion times due to reduced image contrast. As shown, the caudally directed Lagrangian motion in the narrower region of the canal is characterized by a nearly parabolic velocity profile, whereas the flow in the wider region exhibits a more complex structure, as expected given the larger local Womersley number.

While the images in Fig. 2.5 provide clear qualitative evidence of Time-SLIP's ability to track Lagrangian motion, the reduced contrast between the tagged and background fluids complicates accurate quantification of fluid-particle displacements at large inversion times. Using the semi-automated quantification procedure employed in our analysis, the results obtained for TI = 1000, 2000, and 3000 ms show strong internal consistency and excellent agreement with the DNS predictions across most of the canal, independent of axial location and stroke volume. In contrast, images acquired at larger inversion times (TI $\geq$ 4000 ms) lack this level of consistency, with some measured displacements failing to exhibit the expected trends. For this reason, the systematic evaluation of the Lagrangian displacement in Fig. 2.6 is limited to three oscillatory cycles.

The results reveal several flow features that are consistent with previous theoretical predictions [3, 4]. In particular, the magnitude of the Lagrangian displacement increases with increasing stroke volume, with an approximately quadratic dependence. This behavior is demonstrated in Fig. 2.6 by plotting the variation of the medial-axis displacement on both sides of the spinal cord after one (δ_1), two (δ_2), and three (δ_3) cycles as a function of the local stroke volume V_s, together with curves showing the corresponding parabolic fits.

This quadratic scaling can be understood by noting that all experiments are conducted at the same frequency (1 Hz), so the oscillatory velocity that dominates motion in the spinal-canal

phantom scales linearly with stroke volume. In contrast, the small steady secondary velocity that drives the mean Lagrangian drift is proportional to products of the oscillatory velocity and its spatial derivatives [4], and therefore scales with the square of the stroke volume. This trend is clearly reflected in the mean Lagrangian displacements for all three inversion times shown in the figure.

As expected, the Lagrangian displacement of the fluid increases with the number of cycles, i.e. $\delta_3 > \delta_2 > \delta_1$. An estimate of the displacement per cycle, δ_c, at a given axial location can be obtained by dividing the displacement measured for a given inversion time by the corresponding number of cycles, i.e. $\delta_c = (\delta_1, \delta_2/2, \delta_3/3)$, with results shown in Fig. 2.6b.

The results exhibit non-negligible differences among the estimated cyclic displacements, particularly for experiments with relatively large stroke volumes. Specifically, on the wider side of the canal, δ_c tends to increase with the number of cycles, whereas the opposite trend is observed on the narrower side. This behavior can be attributed to axial non-uniformity in the canal geometry. On the wider (narrower) side, each cycle advects a fluid particle closer to (farther from) the entrance, placing it in a region where the local stroke volume is slightly higher (lower), so that subsequent cyclic displacements increase (decrease) in magnitude. This effect, which is clearly significant in the phantom measurements owing to the relatively large stroke volumes, is expected to be negligibly small for *in vivo* measurements of the human spinal canal, where the cyclic displacements have been estimated to be a fraction of a millimeter.

The quantitative information on signal-to-noise ratio presented in Fig. 2.7 allows us to assess several important aspects of Time-SLIP relevant to its potential use as a tool to quantify Lagrangian drift in clinical settings. These include confidence in tagged-fluid detection near walls, uncertainty in displacement measurements and its dependence on stroke volume, and the choice and comparison of inversion times (TI). The detailed color maps showing the spatial distributions of SNR for different inversion times and stroke volumes, summarized in the top and lateral panels, lead to the following conclusions: (i) The signal quality degrades near the bounding walls, particularly near the flexible tube, where consistently low SNR values are observed regardless of TI and V_s.

(ii) The SNR peaks for the smallest stroke volume considered, $V_s = 2.9$ mL. (iii) As expected, the SNR is directly linked to the bolus–background contrast, which peaks at approximately 2500 ms (see Fig. 2.2a). Correspondingly, the SNR reaches its largest values at TI = 2000 and 3000 ms. As shown in the logarithmic bar graphs on both sides of Fig. 2.7, for larger inversion times the SNR decreases sharply, accounting for less consistent displacement estimates at those longer inversion times.

The phantom study has demonstrated the capability of Time-SLIP to reliably identify the cyclic displacements of a tagged fluid region over successive oscillatory cycles. Uncertainties associated with the application of this method in clinical settings arise primarily from differences between the phantom and the human spinal canal. In particular, the smaller width of the latter (approximately 2–4 mm, compared to $(R_o - R_i)/2 = 6$ mm in our annular tube), together with the presence of microanatomical features such as nerve roots, denticulate ligaments, and trabeculae, is expected to hinder the quantification of tagged-bolus displacements. These limitations are anticipated to be most pronounced near the walls, where the SNR has been shown to be small.

Our *in vitro* Time-SLIP study has successfully quantified Lagrangian displacements for inversion times up to TI = 3000 ms, corresponding to three cardiac cycles. The expected Lagrangian displacements in the human spinal canal are on the order of $\delta_3 \sim 1$ mm [6], so characterizing such small displacements will be challenging and will likely require improvements in both imaging and post-processing techniques beyond those implemented here. As shown in Fig. 2.7, the peak signal-to-noise ratio (SNR) occurs for the smallest stroke volume considered, $V_s = 2.9$ mL, a value comparable to, though somewhat larger than, stroke volumes typically reported for the spinal canal ($V_s \sim 1$ mL), which provides some confidence in the feasibility of these measurements. Moreover, increasing the magnetic field strength of the scanner—these experiments were conducted using a 3-Tesla MRI system—could further enhance band-to-background contrast at longer inversion times, thereby enabling the use of larger TI values and the characterization of displacements over a greater number of cycles.

It is also worth noting that the phantom experiments presented here have focused on

Lagrangian flow driven by the cardiac cycle. In contrast, motion in the lumbar region—which is responsible for the initial spreading of intrathecal drugs injected at the L2–L3 level—is known to exhibit a significant contribution from respiratory effects [10]. These effects should be addressed in future studies, bearing in mind that, given the inversion times currently available, Time-SLIP is expected to be able to track the tagged bolus over at least a complete respiratory cycle.

2.5 Conclusion

The phantom experiments presented here demonstrate that Time-SLIP MRI can be used to reliably characterize cyclic Lagrangian displacements over multiple oscillatory cycles, yielding results in close agreement with MRI-informed direct numerical simulations. The study clarifies the conditions under which quantitative displacement measurements are robust, including the choice of inversion time, stroke volume, and number of cycles, and highlights the key limitations associated with signal-to-noise ratio and spatial resolution. Together, these results provide a quantitative foundation for future *in vivo* Time-SLIP investigations aimed at assessing mean Lagrangian motion in the human spinal canal.

2.6 Acknowledgment

Chapter 2, in full, is a reprint of the material as it appears in Campos, O., Alaminos-Quesada, J., Sincomb, S., Malis, V., Miyazaki, M., Coenen, W., Gutiérrez-Montes, C., Martínez-Bazán, C., Pawlak, G., & Sánchez, A. L. (2026). Phantom-Based Evaluation of Time-SLIP MRI for Measuring Spinal-Canal Lagrangian Drift.*(submitted to Scientific Reports)*.The dissertation author was the primary investigator and author of this paper.

Bibliography

[1] Linninger AA, Tangen K, Hsu CY, Frim D. Cerebrospinal fluid mechanics and its coupling to cerebrovascular dynamics. Annu Rev Fluid Mech. 2016;48:219–257.

[2] Kelley DH, Thomas JH. Cerebrospinal fluid flow. Annu Rev Fluid Mech. 2023;55.

[3] Sánchez AL, Martínez-Bazan C, Gutiérrez-Montes C, Criado-Hidalgo E, Pawlak G, Bradley W, et al. On the bulk motion of the cerebrospinal fluid in the spinal canal. J Fluid Mech. 2018;841:203–227.

[4] Lawrence JJ, Coenen W, Sánchez AL, Pawlak G, Martínez-Bazán C, Haughton V, et al. On the dispersion of a drug delivered intrathecally in the spinal canal. J Fluid Mech. 2019;861:679–720.

[5] Coenen W, Gutiérrez-Montes C, Sincomb S, Criado-Hidalgo E, Wei K, King K, et al. Subject-Specific Studies of CSF Bulk Flow Patterns in the Spinal Canal: Implications for the Dispersion of Solute Particles in Intrathecal Drug Delivery. Am J Neuroradiol. 2019;40:1242–1249.

[6] Parras-Martos F, Sánchez A, Martínez-Bazán C, Coenen W, Gutiérrez-Montes C. On reduced-order modeling of drug dispersion in the spinal canal. Fluids and Barriers of the CNS. 2025;22(1):66.

[7] di Chiro G. Movement of the cerebrospinal fluid in human beings. Nature. 1964;204(4955):290–291.

[8] Feinberg DA, Mark AS. Human brain motion and cerebrospinal fluid circulation demonstrated with MR velocity imaging. Radiology. 1987;163(3):793–799.

[9] Sincomb S, Coenen W, Gutiérrez-Montes C, Bazán CM, Haughton V, Sánchez A. A one-dimensional model for the pulsating flow of cerebrospinal fluid in the spinal canal. J fluid Mech. 2022;939:A26.

[10] Gutiérrez-Montes C, Coenen W, Vidorreta M, Sincomb S, Martínez-Bazán C, Sánchez AL, et al. Effect of normal breathing on the movement of CSF in the spinal subarachnoid space. AJNR Am J Neuroradiol. 2022;43(9):1369–1374.

[11] Sincomb S, Coenen W, Criado-Hidalgo E, Wei K, King K, Borzage M, et al. Transmantle pressure computed from mr imaging measurements of aqueduct flow and dimensions. American Journal of Neuroradiology. 2021;42(10):1815–1821.

[12] Karki P, Murphy MC, Ganji S, Gunter JL, Graff-Radford J, Jones DT, et al. Real-Time 2D Phase-Contrast MRI to Assess Cardiac-and Respiratory-Driven CSF Movement in Normal Pressure Hydrocephalus. J Neuroimag. 2025;35(1):e70000.

[13] Yamada S, Tsuchiya K, Bradley W, Law M, Winkler M, Borzage M, et al. Current and emerging MR imaging techniques for the diagnosis and management of CSF flow disorders: a review of phase-contrast and time–spatial labeling inversion pulse. American journal of neuroradiology. 2015;36(4):623–630.

[14] Greitz D, Hannerz J. A proposed model of cerebrospinal fluid circulation: observations with radionuclide cisternography. AJNR Am J Neuroradiol. 1996;17(3):431–438.

[15] S Y. Cerebrospinal fluid dynamics. Croat Med J. 2021;.

[16] Yamada S. Cerebrospinal fluid physiology: visualization of cerebrospinal fluid dynamics using the magnetic resonance imaging Time-Spatial Inversion Pulse method. Croatian medical journal. 2014;55(4):337–346.

[17] Yamada S, Miyazaki M, Kanazawa H, Higashi M, Morohoshi Y, Bluml S, et al. Visualization of cerebrospinal fluid movement with spin labeling at MR imaging: preliminary results in normal and pathophysiologic conditions. Radiology. 2008;249(2):644–652.

[18] Nishimura DG, Macovski A, Pauly JM. Considerations of magnetic resonance angiography by selective inversion recovery. Magnetic resonance in medicine. 1988;7(4):472–484.

[19] Edelman RR, Mattle H, Kleefield J, Silver MS. Quantification of blood flow with dynamic MR imaging and presaturation bolus tracking. Radiology. 1989;171(2):551–556.

[20] Mai VM, Berr SS. MR perfusion imaging of pulmonary parenchyma using pulsed arterial spin labeling techniques: FAIRER and FAIR. Journal of Magnetic Resonance Imaging: An Official Journal of the International Society for Magnetic Resonance in Medicine. 1999;9(3):483–487.

[21] Kanazawa H, Miyazaki M. Time-spatial labeling inversion tag (t-SLIT) using a selective IR-tag on/off pulse in 2D and 3D half-Fourier FSE as arterial spin labeling. Proceedings of the 10th International Society for magnetic Resonance in Medicine, 2002. 2002;140.

[22] Ito K, Koike S, Jo C, Shimizu A, Kanazawa H, Miyazaki M, et al. Intraportal venous flow distribution: evaluation with single breath-hold ECG-triggered three-dimensional half-Fourier fast spin-echo MR imaging and a selective inversion-recovery tagging pulse. American Journal of Roentgenology. 2002;178(2):343–348.

[23] Yamada S, Miyazaki M, Yamashita Y, Ouyang C, Yui M, Nakahashi M, et al. Influence of respiration on cerebrospinal fluid movement using magnetic resonance spin labeling. Fluids Barries CNS. 2013;10(1):36.

[24] Ishibe T, Senzoku F, Kamba Y, Ikeda N, Mikawa Y. Time-spatial labeling inversion pulse magnetic resonance imaging of cystic lesions of the spinal cord. World Neurosurgery. 2016;88:693–e13.

[25] Takeuchi K, Ono A, Hashiguchi Y, Misawa H, Takahata T, Teramoto A, et al. Visualization of cerebrospinal fluid flow in syringomyelia through noninvasive magnetic resonance imaging with a time-spatial labeling inversion pulse (Time-SLIP). The Journal of Spinal Cord Medicine. 2017;40(3):368–371.

[26] Inoue T, Joko M, Murayama K, Ikedo M, Saito F, Muto J, et al. Time-spatial labeling inversion pulse (time-SLIP) MRI for evaluating cerebrospinal fluid velocity and visualizing flow dynamics in patients with Chiari type I malformation. Neurosurgery Practice. 2023;4(4):e00065.

[27] Tomita Y, Yagi M, Seki F, Komaki Y, Suzuki S, Watanabe K, et al. The significance of cerebrospinal fluid dynamics in adolescent idiopathic scoliosis using time-SLIP MRI. Scientific reports. 2024;14(1):12214.

[28] Kelly EJ, Yamada S. Cerebrospinal fluid flow studies and recent advancements. In: Seminars in Ultrasound, CT and MRI. vol. 37. Elsevier; 2016. p. 92–99.

[29] Shiodera T, Nitta S, Takeguchi T, Yui M, Yamashita Y, Yamamoto T, et al. Automated flow quantification for spin labeling MR imaging. Magnetic Resonance Materials in Physics, Biology and Medicine. 2014;27(5):425–433.

[30] Hirayama A, Matsumae M, Yatsushiro S, Abdulla A, Atsumi H, Kuroda K. Visualization of pulsatile CSF motion around membrane-like structures with both 4D velocity mapping and Time-SLIP technique. Magnetic Resonance in Medical Sciences. 2015;14(4):263–273.

[31] Hosotani K, Ono A, Takeuchi K, Hashiguchi Y, Nagahata T. Flow Visualization of Pipe Flows Obtained by MR Imaginary. In: Fluids Engineering Division Summer Meeting. vol. 57230. American Society of Mechanical Engineers; 2015. p. V02AT10A007.

[32] Fukumoto W, Higaki T, Matsuoka Y, Tatsugami F, Baba Y, Iida M, et al. Quantification of the salivary volume flow rate in the parotid duct using the time-spatial labeling inversion pulse (Time-SLIP) technique at MRI: A feasibility study. Journal of Magnetic Resonance Imaging. 2018;47(4):928–935.

[33] Hoshi H, Sugita R, Machida Y. Using spin-labeled MR imaging to depict slow pancreatic juice flow. Magnetic Resonance in Medical Sciences. 2023;22(3):361–371.

[34] Gutiérrez MMP, Gómez YJM, Pulgarín EH, López MEL. Effect of boundary conditions in pressure drop and velocity profiles in aqueduct of Sylvius. IFAC-PapersOnLine. 2018;51(27):294–298.

[35] Khani M, Sass LR, Xing T, Keith Sharp M, BalÃ©dent O, Martin BA. Anthropomorphic Model of Intrathecal Cerebrospinal Fluid Dynamics Within the Spinal Subarachnoid Space: Spinal Cord Nerve Roots Increase Steady-Streaming. Journal of Biomechanical Engineeing. 2018 06;140(8):081012.

[36] Tangen K, Nestorov I, Verma A, Sullivan J, Holt RW, Linninger AA. In Vivo Intrathecal Tracer Dispersion in Cynomolgus Monkey Validates Wide Biodistribution Along Neuraxis. IEEE Transactions on Biomedical Engineering. 2020;67(4):1122–1132.

[37] Gutiérrez-Montes C, Coenen W, Lawrence JJ, Martínez-Bazan C, Sánchez AL, Lasheras JC. Modelling and direct numerical simulation of flow and solute dispersion in the spinal subarachnoid space. Applied Mathematical Modelling. 2021;94:516–533. Available from: https://www.sciencedirect.com/science/article/pii/S0307904X21000548.

[38] Alaminos-Quesada J, Gutiérrez-Montes C, Coenen W, Sánchez AL. Effects of buoyancy on the dispersion of drugs released intrathecally in the spinal canal. Journal of Fluid Mechanics. 2024;985:A20.

[39] Alaminos-Quesada J, Coenen W, Gutiérrez-Montes C, Sánchez AL. Buoyancy-modulated Lagrangian drift in wavy-walled vertical channels as a model problem to understand drug dispersion in the spinal canal. Journal of Fluid Mechanics. 2022;949:A48.

Part II

Engineering Physiologically Relevant Flow Environments for Pulmonary Arterial Endothelial Studies

Chapter 3

A Multi-Chamber Pulsating-Flow Device with Optimized Spatial Shear Stress and Pressure for Endothelial-Cell Testing

Endothelial cells line the interior of arteries and respond to cyclic mechanical loads generated by the cardiovascular flow dynamics including shear stress, pressure, and stretching [1, 2]. Mechanosensors on endothelial cells detect these forces and transduce them into biochemical signals that trigger vascular responses [3]. In fact, the regulation of endothelial gene expression through biomechanical forces is a critical determinant of normal vascular homeostasis. However, alterations in mechanical forces associated with vascular remodeling and/or aberrant vascular architecture disrupt these normal responses, and result in endothelial dysfunction and vascular diseases. For example, alterations in mechanical forces secondary to congenital heart disease predispose the pulmonary circulation to the development of pulmonary hypertension [4]. Current research on pulmonary arterial endothelial cells aims to identify the key genes expressed under conditions of heightened hemodynamic mechanical loads that participate in abnormal pulmonary vascular remodeling. The long-term goal of these studies is the development of pharmaceuticals that can mitigate deleterious response in endothelial cells. These strategies effectively aim to extend the lives of children born with congenital heart diseases who subsequently develop pulmonary hypertension. Unfortunately, the current in vitro assessment of mechanical forces is flawed and problematic. Most notable, the inability to control, isolate and coordinate crucial mechanical forces, presents formidable challenges to understanding disease etiologies.

Here, we present the design, development, and testing of the Multiplex Cell Shearer (MCS),

a new device inspired by the need for in vitro experiments where cells are subjected to carefully controlled pressure and shear stress. The apparatus utilized in these experiments must be biocompatible and capable of accommodating a significant cell population suitable for bulk RNA sequencing. This device must expose the cells located within a designated testing region to spatially uniform wall shear stress and pressure during pulsatile flow. Simultaneously, it should enable researchers to expedite experiments by facilitating concurrent testing of different mechanical conditions for cells.

Previous studies have used a variety of flow chamber designs to study the response of endothelial cells to shear stress (see the recent papers by Fallon et al. [5] and Meng et al. [6] for thorough reviews of relevant literature). The most commonly used device is the parallel-plate flow chamber, which is to be considered in our analysis. These chambers feature two parallel plates separated by a narrow gap, forming a Hele-Shaw cell [7] through which flow is driven via inlet and outlet ports positioned at opposite ends. The rectangular coverslip containing the endothelial cells is typically placed in the center region, flush with the bottom plate away from the feeding ports, where the streamlines are nearly parallel. Since the inter-plate (typically 1 mm) distance is much larger than the thickness of the endothelial cells (about 0.1-10 μm [8, 9]), the presence of the latter does not significantly perturb the flow. Therefore, the shear stress felt by cells corresponds to the wall shear stress existing in the absence of cells. While most experimental studies have focused on steady flow conditions (e.g., [10]), there is ample evidence that the response of endothelial cells depends critically on the flow unsteadiness [5], thereby motivating investigations accounting for pulsatile flow, including realistic arterial waveforms, as needed to mimic physiological conditions.

Theoretical analyses are useful for generating quantitative predictions associated with flow chambers of given geometry. The simplest description assumes two infinite parallel plates separated by a distance $2h$ subject to a longitudinal pressure gradient with angular frequency ω, yielding a unidirectional solution that depends on the Womersley number

$$M = \left(\frac{\rho\omega h^2}{\mu}\right)^{1/2}, \tag{3.1}$$

where ρ and μ are the density and dynamic viscosity of the fluid. As discussed by Fallon et

al. [5], for small values of M, corresponding to the conditions found in small arteries, the solution reduces to the familiar Poiseuille solution [7]. Effects of local acceleration become important for increasing values of M, resulting in values of the shear stress that depart from those of the steady Poiseuille solution [11–14]. Extensions of the planar Womersley solution exist for the case of an infinitely long channel with a rectangular cross section [15].

For the cells in a given experiment to be subject to the same shear stress, they have to be placed in a region where the unidirectional flow is fully developed. The streamwise distance needed to establish the unidirectional flow has been determined analytically and numerically for the case of a two-dimensional channel [16–21]. In order to ensure uniform shear stress for realistic flow chambers, characterizing the spatial distribution of shear stress corresponding to a given planform is necessary. A first step in that direction was taken by Qin et al. [22], who considered in particular planforms corresponding to a complex velocity potential with a presumed power-law. Here, we generalize their analysis for plates of arbitrary shape. Additionally, we use the theoretical predictions to characterize the flow in parallel-plate chambers of hexagonal planform. These results are used to guide the design of a new device, the Multiplex Cell Shearer (MCS). To isolate the effects of different mechanical stimuli, there is an interest in subjecting the cells to the same cyclic shear stress but with pressure fluctuations of differing amplitudes. This is achieved in the MCS by connecting four identical parallel-plate chambers in series. Cells experience the same wall shear stress in all four chambers with four different pressure ranges. Experimental flow diagnostics are then used to validate the theoretical predictions and characterize the temporal and spatial pressure fluctuations experienced by the cells.

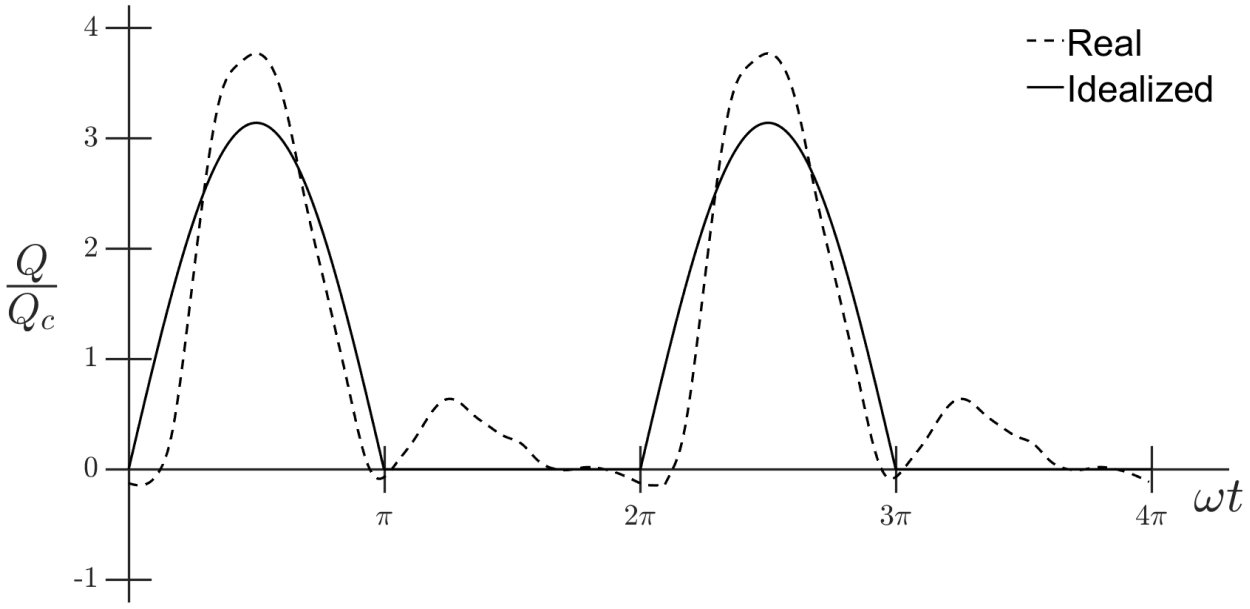

Figure 3.1: Comparison of the flow rate waveform used in experiments (solid curve) with that measured in the main pulmonary artery (dashed curve) [23].

3.1 Unsteady Viscous Flow in Parallel-Plate Flow Chambers of General Planform

3.1.1 Problem Statement

To guide the design of the device, we begin by investigating unsteady viscous flow in parallel-plate channels. The following analysis is valid for devices of arbitrary planform and for general flow rate waveforms. Specific results will be presented for a simplified flow rate waveform that mimics those encountered in the pulmonary arteries [23], shown in dimensionless form in Fig. 3.1. The idealized waveform captures the general physiologically relevant features in the flow rate profile and allows for better experimental control. We will consider a hexagonal planform for our flow chamber with a length $2L$, width $2W$, and semi-angle α (see Fig. 3.2).

It is assumed that the two parallel plates bounding the channel are separated by a small distance $2h$, with $h \ll W \sim L$. The coverslip containing the cells is placed at the center of the bottom plate. The working fluid flows through inlet and outlet ports of diameter $D \ll L$ located

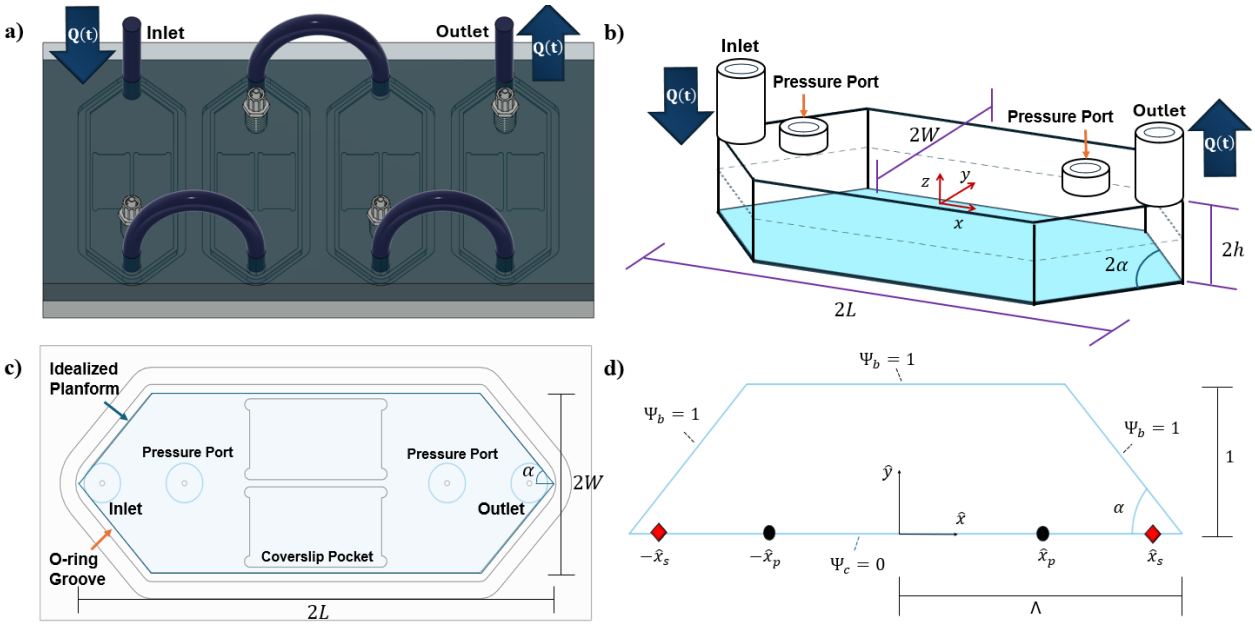

Figure 3.2: A schematic view of the Multiplex Cell Shear (MCS) (a) and of the individual chamber (b) and its planform (c). Panel (d) shows the numerical domain and boundary conditions for integration of Eq. (3.18), with the symbols along the horizontal axis denoting the location of the singularities $\pm\hat{x}_s$, representing the inlet and outlet ports, and well as the location of the pressure ports $\pm\hat{x}_p$.

on the upper plate near the lengthwise vertices. In the analysis, the working fluid is assumed to be Newtonian with density ρ and dynamic viscosity μ similar to those of water at 37C, as is appropriate for the low concentration of glucose and other additives present in the cell media typically used in in vitro experiments.

In the experiments, a pulsatile pump drives a prescribed time-periodic flow rate

$$Q(t)/Q_c = \mathrm{Re}\left(\sum_{n=0}^{\infty} A_n \mathrm{e}^{\mathrm{i}n\omega t}\right), \tag{3.2}$$

where Re represents the real part of a complex function, ω is the fundamental angular frequency of the cardiac cycle, A_n are dimensionless complex Fourier series coefficients measuring the amplitude and phase of the different modes, and Q_c denotes a representative value of the flow rate. In the following, we shall use the net flow rate, i.e. the time-averaged value of $Q(t)$ over a period

$$Q_c = \frac{1}{2\pi/\omega}\int_t^{t+2\pi/\omega} Q(t)\mathrm{d}t, \tag{3.3}$$

as a measure of the characteristic flow rate. With this definition, the Fourier series coefficient associated with mode $n = 0$ reduces to $A_0 = 1$.

The problem will be described using Cartesian coordinates (x, y, z) with origin placed at the center of the chamber, as indicated in Fig. 3.2b, and corresponding velocity components (u, v, w). The spatial pressure difference (e.g. measured from the origin of the reference frame) will be denoted by p. The flow near the inlet and outlet ports can be expected to be fully three dimensional, all three velocity components having comparable magnitude. Since the cells are placed near the center of the device, there is little interest in describing the complicated flow existing in these near-port regions. Attention is focused instead on the main region away from the ports, i.e. at distances from the vertices much larger than D, where the streamlines are parallel to the bounding plates (i.e. $w \simeq 0$), thereby enabling a simplified description of the Hele-Shaw type to be performed. Of particular interest for our application is the value of the wall shear stress in the testing region

$$\tau_x = \mu \left.\frac{\partial u}{\partial z}\right|_{z=-h} \quad \text{and} \quad \tau_y = \mu \left.\frac{\partial v}{\partial z}\right|_{z=-h} \tag{3.4}$$

and its connection with the flow rate Eq. (3.2) and chamber geometry.

3.1.2 Simplifying Assumptions

In the main flow region away from the ports, the conservation equations admit a number of simplifications. Since the streamlines are parallel to the confining walls (i.e. $w = 0$), it follows that $\partial p/\partial z = 0$, thereby yielding $p(x, y, t)$. Furthermore, since $h \ll W \sim L$, only the transverse derivatives need be accounted for when evaluating viscous forces, terms involving second derivatives in x and y being a factor of order $(h/W)^2$ smaller. It will be assumed that convective acceleration has a negligible effect for the flow conditions investigated here, because the relevant lubrication Reynolds number satisfies

$$\frac{\rho u_c h}{\mu}\frac{h}{W} \ll 1, \tag{3.5}$$

where $u_c = Q_c/(2hW)$ is the characteristic streamwise velocity. On the other hand, in practical applications the characteristic viscous time $h^2/(\mu/\rho)$ is comparable to the characteristic oscillation time ω^{-1}, yielding order-unity values of the Womersley number M defined in Eq. (3.1), with the result that effects of local acceleration can be expected to be important.

The above approximations effectively reduce the problem to one involving the unsteady form of the lubrication equations, written in dimensionless form as

$$\frac{\partial \hat{u}}{\partial \hat{x}} + \frac{\partial \hat{v}}{\partial \hat{y}} = 0 \tag{3.6}$$

$$M^2 \frac{\partial \hat{u}}{\partial \hat{t}} = -\frac{\partial \hat{p}}{\partial \hat{x}} + \frac{\partial^2 \hat{u}}{\partial \hat{z}^2} \tag{3.7}$$

$$M^2 \frac{\partial \hat{v}}{\partial \hat{t}} = -\frac{\partial \hat{p}}{\partial \hat{y}} + \frac{\partial^2 \hat{v}}{\partial \hat{z}^2} \tag{3.8}$$

in terms of $\hat{t} = \omega t$, $\hat{x} = x/W$, $\hat{y} = y/W$, $\hat{z} = z/h$, $\hat{u} = u/u_c$, $\hat{v} = v/u_c$, and $\hat{p} = p/(\mu u_c W/h^2)$. The velocity must satisfy the no-slip conditions

$$\hat{u} = \hat{v} = 0 \quad \text{at} \quad \hat{z} = \pm 1. \tag{3.9}$$

With the second order spatial derivatives in the $\hat{x}$ and $\hat{y}$ directions neglected in Eqs. (3.7) and (3.8), the outer walls delineating the hexagon become stream surfaces with non-zero slip velocity, to be computed as part of the description. The flow rate must be equal to the value specified above in Eq. (3.2). For example, evaluating the flow rate at $x = 0$ provides the integral constraint

$$\hat{Q}(\hat{t}) = Q(t)/Q_c = \int_0^1 \left(\int_{-1}^1 \hat{u} \mathrm{d}\hat{z} \right) \mathrm{d}\hat{y} = \mathrm{Re}\left(\sum_{n=0}^{\infty} A_n \mathrm{e}^{\mathrm{i}n\hat{t}} \right), \tag{3.10}$$

where the integral in $\hat{y}$ is extended over half of the domain, as is appropriate given the symmetry of the problem.

3.1.3 General Solution

The linear problem defined above depends on the Womersley number M, the complex dimensionless factors A_n, and the geometry of the planform, described by the semi-angle α and the aspect ratio $\Lambda = L/W$. A closed-form solution is sought by introducing the ansatz

$$\hat{p} = \mathrm{Re}\left(\sum_{n=0}^{\infty} B_n \mathrm{e}^{\mathrm{i}n\hat{t}}\right)\phi(\hat{x},\hat{y}), \tag{3.11}$$

involving the complex constants B_n and the real function $\phi(\hat{x},\hat{y})$. The accompanying velocity is given by

$$\frac{(\hat{u},\hat{v})}{\mathrm{Re}\left(\sum_{n=0}^{\infty} B_n \mathrm{e}^{\mathrm{i}n\hat{t}} G_n(\hat{z})\right)} = \left(\frac{\partial\phi}{\partial\hat{x}}, \frac{\partial\phi}{\partial\hat{y}}\right), \tag{3.12}$$

where

$$G_n = \frac{\mathrm{i}}{nM^2}\left[1 - \frac{\cosh(\sqrt{\mathrm{i}n}M\hat{z})}{\cosh(\sqrt{\mathrm{i}n}M)}\right], \tag{3.13}$$

describing the transverse variation of the velocity, is obtained by integrating the problem

$$\mathrm{i}nM^2 G_n = -1 + \frac{\mathrm{d}^2 G_n}{\mathrm{d}\hat{z}^2}, \quad G_n(\pm 1) = 0 \tag{3.14}$$

arising from Eqs. (3.7) and (3.8).

The form of Eq. (3.12) indicates that $\hat{v}/\hat{u}$ is independent of $\hat{z}$, so that the streamline pattern is identical in different planes of constant $\hat{z}$. Furthermore, since

$$\frac{\partial\hat{v}}{\partial\hat{x}} - \frac{\partial\hat{u}}{\partial\hat{y}} = 0, \tag{3.15}$$

at any given $\hat{z}$ the flow is effectively irrotational, with the function ϕ representing a reduced velocity potential. Since the integral constraint given in Eq. (3.10) involves the flow rate, to facilitate the

solution it is convenient to express the velocity

$$(\hat{u}, \hat{v}) = \mathrm{Re}\left[\sum_{n=0}^{\infty} B_n \mathrm{e}^{\mathrm{i}n\hat{t}} G_n(\hat{z})\right]\left(\frac{\partial\psi}{\partial\hat{y}}, -\frac{\partial\psi}{\partial\hat{x}}\right), \tag{3.16}$$

in terms of the stream function $\psi(\hat{x}, \hat{y})$, related to the velocity potential by

$$\frac{\partial\phi}{\partial\hat{x}} = \frac{\partial\psi}{\partial\hat{y}} \quad \text{and} \quad \frac{\partial\phi}{\partial\hat{y}} = -\frac{\partial\psi}{\partial\hat{y}}. \tag{3.17}$$

As can be seen by substituting Eq. (3.16) into Eq. (3.15), the stream function satisfies Laplace's equation

$$\frac{\partial^2\psi}{\partial\hat{x}^2} + \frac{\partial^2\psi}{\partial\hat{y}^2} = 0. \tag{3.18}$$

The value of ψ must be constant along the planform boundaries, which are streamlines of the flow. Because of the planform symmetry, the problem can be solved by considering half of the flow domain, as indicated in Fig. 3.2d. According to Eq. (3.10), the value ψ_c of ψ along the centerline connecting the two ports and that along the planform boundary (ψ_b) are related by $A_n = (\psi_b - \psi_c)B_n q_n$, where

$$q_n = \int_{-1}^{1} G_n(\hat{z})\,\mathrm{d}\hat{z} = \frac{2\mathrm{i}}{nM^2}\left[1 - \frac{\tanh(\sqrt{\mathrm{i}n}M)}{\sqrt{\mathrm{i}n}M}\right]. \tag{3.19}$$

In the following, we choose $\psi_c = 0$ and $\psi_b = 1$, as indicated in Fig. 3.2d, so that

$$B_n = A_n/q_n \tag{3.20}$$

and $B_0 = -(3/2)A_0$ for $n = 0$.

In defining boundary conditions for integrating Eq. (3.18), additional care must be taken to describe the near-port inflow and outflow regions. For the specific case considered here, the diameter of the feeding ports D satisfies $D \ll W$. Therefore, the inlet and outlet can be modeled as a point source located at $\hat{x} = -\hat{x}_s$ and a point sink located at $\hat{x} = \hat{x}_s$, respectively, with $\hat{x}_s < \Lambda$.

Near these singularities the stream function takes the asymptotic form

$$\psi \to \frac{1}{\pi}\tan^{-1}\left(\frac{\hat{y}}{\hat{x}_s \mp \hat{x}}\right). \tag{3.21}$$

Once the stream function is obtained by integration of Eq. (3.18), the result can be used in Eq. (3.16) to evaluate the velocity, and in Eq. (3.17) to evaluate the pressure gradient

$$\left(\frac{\partial \hat{p}}{\partial \hat{x}}, \frac{\partial \hat{p}}{\partial \hat{y}}\right) = \mathrm{Re}\left(\sum_{n=0}^{\infty} B_n \mathrm{e}^{\mathrm{i}n\hat{t}}\right)\left(\frac{\partial \psi}{\partial \hat{y}}, -\frac{\partial \psi}{\partial \hat{x}}\right), \tag{3.22}$$

with the Fourier coefficients B_n determined with use of Eq. (3.20). The velocity profile is needed, in particular, to compute the shear stress experienced by the cells with the use of Eq. (3.4). Using the dimensionless form $(\hat{\tau}_x, \hat{\tau}_y) = (\tau_x, \tau_y)/(\mu u_c/h)$, consistent with the scales used in the paper, it follows that

$$\left(\hat{\tau}_x, \hat{\tau}_y\right) = \mathrm{Re}\left(\sum_{n=0}^{\infty} C_n \mathrm{e}^{\mathrm{i}n\hat{t}}\right)\left(\frac{\partial \psi}{\partial \hat{y}}, -\frac{\partial \psi}{\partial \hat{x}}\right), \tag{3.23}$$

where

$$C_n = B_n \left.\frac{\mathrm{d}G_n}{\mathrm{d}\hat{z}}\right|_{\hat{z}=-1} = \frac{1}{2}\mathrm{i}nM^2 A_n \left[\frac{\sqrt{\mathrm{i}n}M}{\tanh(\sqrt{\mathrm{i}n}M)} - 1\right]^{-1} \tag{3.24}$$

for $n \leq 1$ and $C_0 = (3/2)A_0$ for $n = 0$. On the other hand, the expressions given in Eq. (3.22) can be integrated to evaluate spatial pressure differences within the chamber. For example, the instantaneous pressure difference between two points placed at symmetric locations $\hat{x} = \pm\hat{x}_p$ along the centerline $\hat{y} = 0$, as indicated in Fig. 3.2d, is given by

$$\Delta\hat{p} = \mathrm{Re}\left(\sum_{n=0}^{\infty} B_n \mathrm{e}^{\mathrm{i}n\hat{t}}\right)\int_{-\hat{x}_p}^{\hat{x}_p} \frac{\partial \psi}{\partial \hat{y}}\mathrm{d}\hat{x}. \tag{3.25}$$

This last expression is to be tested later by comparison with direct experimental measurements.

The expressions given in Eqs. (3.16), (3.22), and (3.23) are product functions. The factors involving derivatives of ψ, identical in all three equations, describe the spatial distribution of velocity, pressure gradient, and shear stress through the planform. They carry the dependence of

the solution on the planform shape through α, Λ, and the singularity locations, $\pm\hat{x}_s$. On the other hand, the factors involving the sums of Fourier modes, describing the temporal variation of the pressure gradient, shear stress, and transverse changes of velocity, carry the dependence of the solution on the Womersley number M and the flow rate waveform. These two distinct components of the solution are to be investigated separately in the following subsections.

3.1.4 Temporal Response of the Velocity, Wall Shear Stress, and Pressure Gradients

For given values of the Womersley number M and of the Fourier coefficients A_n, the latter defining the flow rate according to Eq. (3.2), one can use Eqs. (3.19) and (3.20) to compute the coefficients B_n, which determine the temporal variation of the velocity and the pressure gradient using Eqs. (3.16) and (3.22), and (3.24) to compute the coefficients C_n, which determine through Eq. (3.23) the temporal variation of the wall shear stress. Representative results are given below for two different pulsatile flow rate profiles. The first set of results, shown in Fig. 3.3, corresponds to a flow rate with a sinusoidal variation $\hat{Q} = 1 - \cos\hat{t}$. The second set of results, shown in Fig. 3.4, uses the idealized representation of the main pulmonary arterial flow rate depicted by the solid curve in Fig. 3.1, corresponding to a piecewise waveform defined by $\hat{Q} = \pi \sin\hat{t}$ for $0 < \hat{t} < \pi$ and $\hat{Q} = 0$ for $\pi < \hat{t} < 2\pi$. Because the profile time derivatives are not continuous, the associated Fourier representation requires a large number of modes $N \gg 1$ to ensure high resolution, with N =10,000 used for the results shown in Fig. 3.4.

The plots in Figs. 3.3 and 3.4 compare results for $M = 3$ and $M = 5$ with those of the quasi-steady limit $M \ll 1$. In this limiting case, represented by the dashed curves in Figs. 3.3 and 3.4, the solution reduces to

$$-\mathrm{Re}\left(\sum_{n=0}^{\infty} B_n e^{in\hat{t}}\right) = \mathrm{Re}\left(\sum_{n=0}^{\infty} C_n e^{in\hat{t}}\right) = (3/2)\hat{Q}, \tag{3.26}$$

corresponding to the familiar Poiseuille-flow solution, in which the pressure gradient and shear

stresses are in phase with the flow rate, their waveforms being linearly proportional to one another, as shown in Figs. 3.3 and 3.4. In this quasi-steady limit, the functions G_n defined in Eq. (3.13) reduce to $G_n = -(1 - \hat{z}^2)/2$, so that the velocity profile Eq. (3.16) adopts the parabolic shape

$$(\hat{u}, \hat{v}) = \frac{3}{4}\hat{Q}(1 - \hat{z}^2)\left(\frac{\partial\psi}{\partial\hat{y}}, -\frac{\partial\psi}{\partial\hat{x}}\right). \tag{3.27}$$

As illustrated in the right-hand-side panels of Figs. 3.3 and 3.4, the velocity profiles for $M \geq 1$ differ significantly from the parabolic shape given in Eq. (3.27). Correspondingly, the temporal responses of the pressure gradient, measured by the function $\mathrm{Re}\left(\sum_{n=0}^{\infty} B_n \mathrm{e}^{\mathrm{i}n\hat{t}}\right)$, and of the wall shear stress, measured by the function $\mathrm{Re}\left(\sum_{n=0}^{\infty} C_n \mathrm{e}^{\mathrm{i}n\hat{t}}\right)$, differ markedly from the quasi-steady profiles. Not only is the magnitude of the resulting fluctuations significantly larger, especially in connection with the shear stress, but the waveforms also differ notably from that of the imposed flow rate. The changes are more dramatic for the arterial waveform investigated in Fig. 3.4, which includes a zero flow rate over half of the cycle. During the acceleration phase from rest, which begins to occur at $\hat{t} = 0$, the velocity initially maintains a nearly uniform top-hat profile. Viscous forces are only important near the walls, where a thin boundary layer develops, with the result that the associated shear stress exhibits a sudden jump at $\hat{t} = 0$ to a finite value. The deceleration phase requires an adverse pressure gradient that produces back flow near the walls, as seen in the velocity profile for $\hat{t} = 2\pi$. Correspondingly, the shear stress, which is always positive for $M \ll 1$, becomes negative over part of the cycle. The sudden halt of the flow rate at $\hat{t} = \pi$ is accompanied by a jump in shear stress and pressure gradient. Clearly, the profound differences between the results of Figs. 3.3 and 3.4 underscore the need to use a flow rate with a physiologically correct waveform when characterizing the response of endothelial cells.

3.1.5 Assessment of Spatial Non-Uniformity inside the Testing Region

The design of the experimental apparatus must ensure that the cell substrate within the testing region experiences a uniform shear stress, up to a specified tolerance. This uniformity

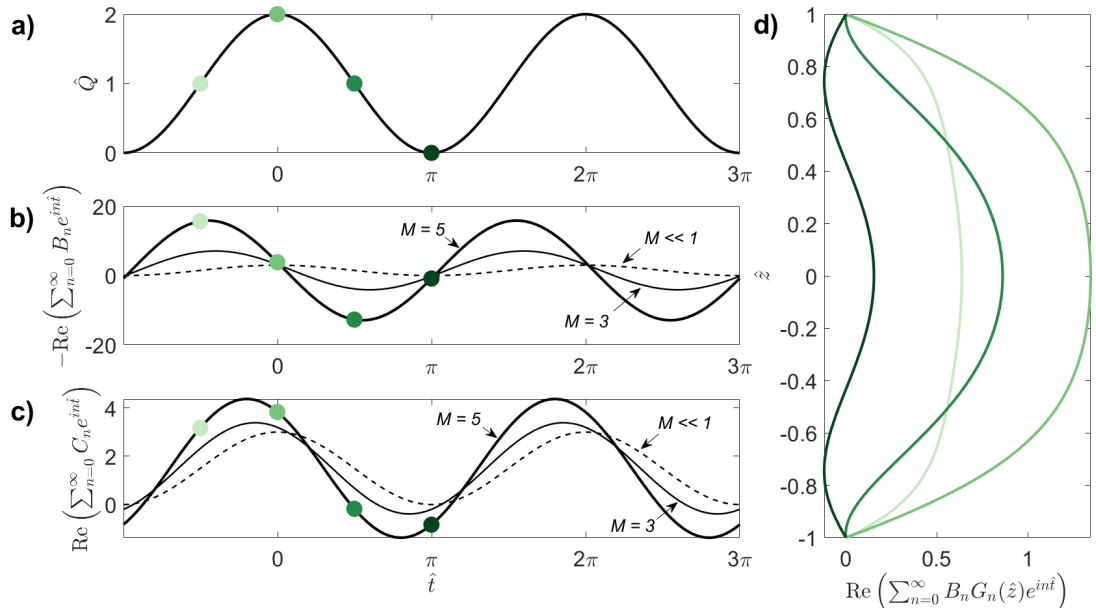

Figure 3.3: Temporal response of the flow corresponding to a pulsatile flow rate $\hat{Q} = 1 - \cos\hat{t}$, including (a) flow rate waveform, (b) pressure gradient, (c) wall shear stress, and (d) velocity profile at different instants of time.

is essential for generating repeatable and reliable data for bulk RNA sequencing of endothelial cells. As can be concluded from Eqs. (3.16), (3.22) and (3.23) the spatial distributions of velocity, pressure gradient and shear stress throughout the chamber are determined by the stream function $\psi(\hat{x}, \hat{y})$. To assess spatial non-uniformity one can use Eq. (3.23) to derive the function

$$\mathcal{T}(\hat{x}, \hat{y}) = \frac{\tau - \tau_o}{\tau_o} = \frac{[(\partial\psi/\partial x)^2 + (\partial\psi/\partial y)^2]^{1/2}}{[(\partial\psi/\partial x)^2 + (\partial\psi/\partial y)^2]^{1/2}|_{(\hat{x}=0,\hat{y}=0)}} - 1, \tag{3.28}$$

which measures the relative departures of the wall-shear-stress magnitude $\tau = \sqrt{\hat{\tau}_x^2 + \hat{\tau}_y^2}$ from its value at the center of the chamber τ_o. As can be concluded from Eqs. (3.16) and (3.22) the same function $\mathcal{T}(\hat{x}, \hat{y})$ characterizes the spatial non-uniformity of the velocity and pressure gradient.

The function $\mathcal{T}$ was used to examine uniformity of the flow within the testing region of our hexagonal planform. The open-source Finite Element Solver (FreeFEM++) was used to evaluate the stream function $\psi(\hat{x}, \hat{y})$ by integration of Eq. (3.18) in the trapezoidal domain of Fig. 3.2d. The results were used to determine $\mathcal{T}$ within the testing region. Sample results, corresponding a

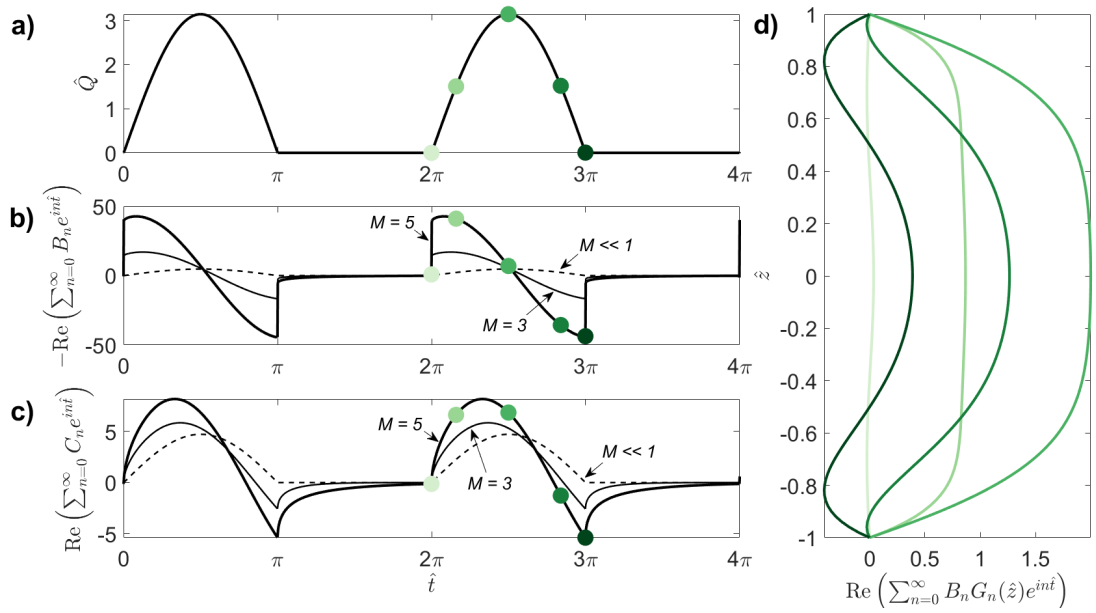

Figure 3.4: Temporal response of the flow corresponding to an idealized representation of the pulmonary arterial flow rate, including (a) flow rate waveform, (b) pressure gradient, (c) wall shear stress, and (d) velocity profile at different instants of time.

chamber with $\alpha = 48°$, $\hat{x}_s = \Lambda - 0.3$, and three different values of the aspect ratio Λ are shown in Fig. 3.5.

As can be seen, for the smallest aspect ratio considered ($\Lambda = 1.7$), corresponding to the minimum value compatible with the angle $\alpha = 48°$ selected in the computations, the spatial nonuniformities are severe, in that cells located near the corners of a coverslip would experience shear stresses that differ from those found near the center by a significant amount. As the aspect ratio increases, the magnitude of $\mathcal{T}$ within the testing region diminishes, reaching values on the order of $\mathcal{T} = 0.1$ for $\Lambda = 2.3$. For the largest aspect ratio ($\Lambda = 2.9$) considered the value of $\mathcal{T}$ was found to be below $\mathcal{T} = 0.02$ everywhere in the testing region. Although the spatial nonuniformity can be further minimized by increasing Λ, the 2% departures associated with $\Lambda = 2.9$ were deemed to be satisfactory for our testing needs. Based on these considerations, the planform shown on the bottom plot of Fig. 3.5 was selected for the design of the chamber.

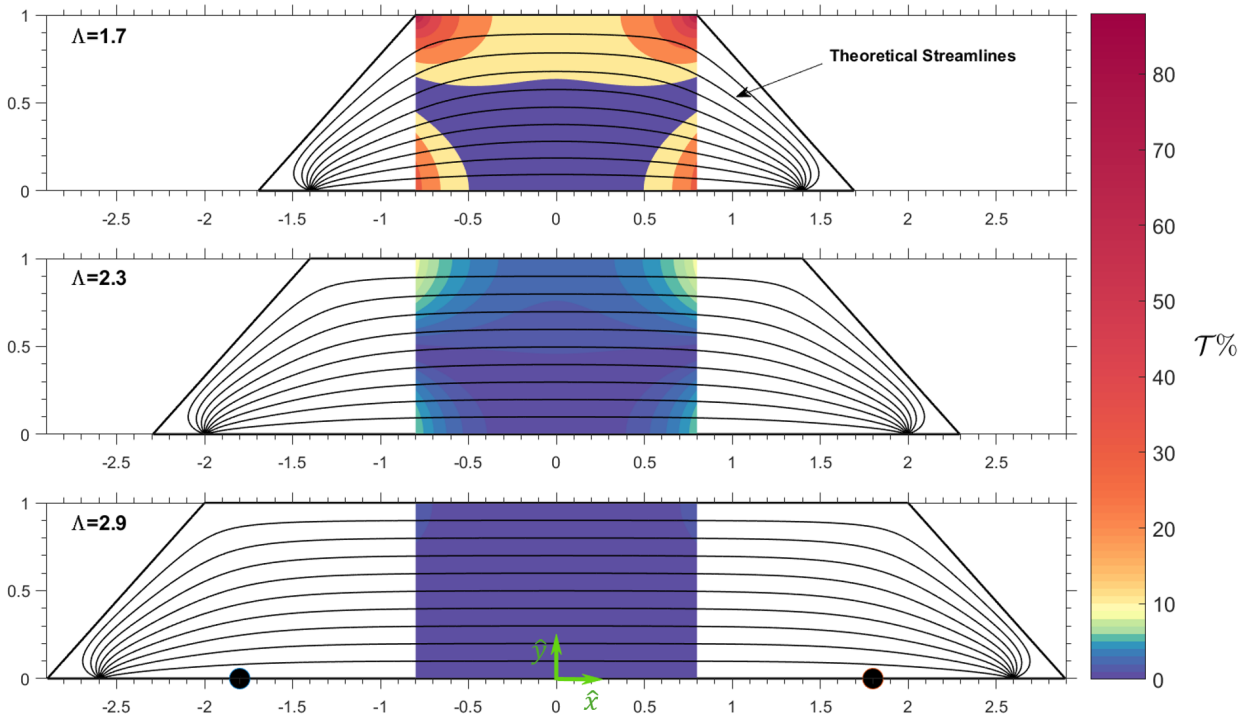

Figure 3.5: The variation of the function $\mathcal{T}$ within the testing region for a hexagonal flow chamber with $\alpha = 48°$, $\hat{x}_s = \Lambda - 0.3$, and three different values of the aspect ratio Λ.

3.2 Multiplex Cell Shearer

The previous section discussed pulsatile flow through a parallel-plate flow chamber with an arbitrary planform, along with the methodology used to analyze the shear-stress spatial non-uniformity present inside a designated testing region of the chamber, which led to the selection of its aspect ratio. Additional details pertaining to the design of the experimental apparatus are provided in the following paragraphs.

3.2.1 Design and Description of Apparatus

The MCS comprises four identical parallel-plate flow chambers connected in series, as depicted in Fig. 3.1. Cells are subjected to the same cyclic shear stress across the device with diminishing pressure ranges in successive chambers. A larger number of chambers is desirable to achieve a greater range in pressures, but this increases preparation time to run the tests. The

maximum number is also limited by pump capacity. For the current design, we chose to use four chambers based on these trade-offs. The four chambers are arranged side by side, with 1/4" reinforced polyvinyl-chloride tubing linking them at their respective ports. The tubing connections are made using 1/4" nominal-pipe-tapered (NPT) threading to 1/4" barb adapters. Notably, the system is entirely rigid apart from the interconnecting tubing, thereby ensuring that the flow rate remains constant in all chambers. According to the results shown in Fig. 3.5, for the aspect ratio $\Lambda = 2.9$ selected in our design, the relative variations of wall shear stress within the testing region can be expected to remain below 2%. In this setup, the pressure drop across the tubing linking the chambers is much larger than the pressure drop associated with the action of viscous shear within each chamber, as shown later in Section 3.3.2. The pressure will thus be nearly uniform in each chamber with cyclical fluctuations of decreasing amplitude in successive chambers. This key feature of the device, to be verified below through experimental measurements, enables experimental tests in which four populations of endothelial cells are subjected to the same shear stress but different pressure fluctuations.

The device is constructed with two plates securely bolted together, with each chamber featuring a watertight seal facilitated by silicone o-rings that are placed within grooves in the bottom plate. The bottom plate also houses the flow pocket, the area where fluid flows through the chamber, consisting of an irregular hexagonal planform as shown in Fig. 3.2. The flow pocket has dimensions $L = 72.5$ mm, $W = 25$ mm, and a semi-angle $\alpha = 48°$. The top plate is equipped with four orifices, each tapped for 1/4" NPT connectors. Among these orifices, the two located at either end serve as inlet and outlet ports, while the inner two orifices function as ports for pressure sensors. The two plates are separated by a distance $2h = 1.2$ mm.

To ensure high precision, the device was manufactured using a computer numerical control (CNC) mill. The lengthwise edges of the flow pocket were rounded to accommodate 1/4" NPT tapered fittings at the inlet and outlet. Then to further ease the manufacturing process, the widthwise edges were rounded to a radius of 1/16". Next, two side-by-side pockets were incorporated at the center-bottom of the flow pocket to facilitate the placement of two coverslips. These coverslip

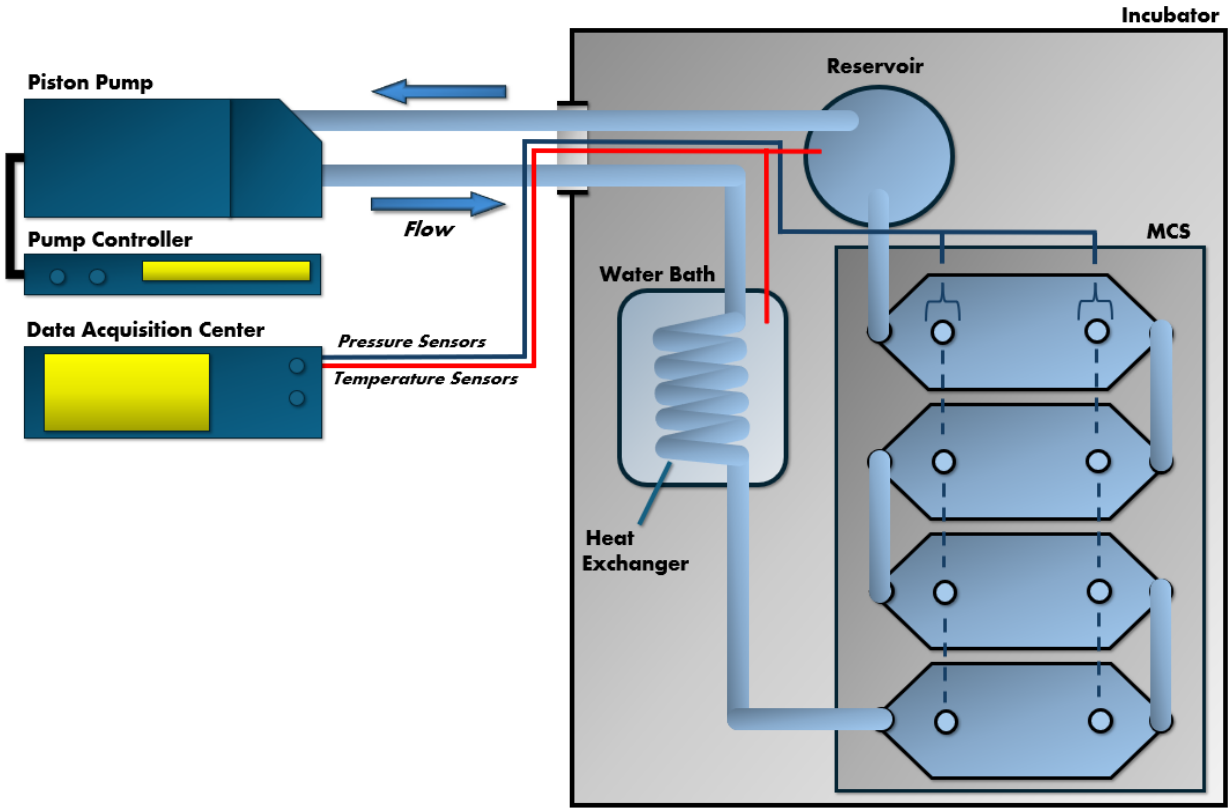

Figure 3.6: Flow system setup used for in vitro experiments.

pockets were designed to accommodate #1.5 thickness coverslips measuring 22 mm x 40 mm. When inserted, the coverslips sit flush with the bottom surface of the flow pocket. The coverslip pockets feature additional grooves for handling. Furthermore, to isolate the coverslips from each other and the wall, a 1.5 mm gap was incorporated on both widthwise ends. The final setup is schematically represented in Fig. 3.2c. A clear acrylic top is used to allow for visual access to the chamber. The bottom plate consists of polypropylene, with a silicone o-ring providing a seal between the two plates. Stainless steel (316) tubing connectors interlink the chambers together with the polyvinyl-chloride tubing. All materials were tested for biocompatibility using a toxicity test with human umbilical vein endothelial cells (HUVECs) and ovine pulmonary arterial endothelial cells (PAECs).

3.2.2 Flow System for Cellular Experiments

The apparatus is an integral part of a comprehensive flow system, which includes a heat exchanger, a reservoir, a piston pump, and a data acquisition system (Fig. 3.6). The heat exchanger comprises 304 stainless steel 3/16" tubing coiled in a spiral configuration, submerged within a water bath maintained at a prescribed temperature. The reservoir used here is a 500 ml glass bottle. The piston pump utilized (SuperPump AR, ViVitro Labs, Victoria, Canada) is capable of delivering a user-defined flow rate waveform at a predetermined cycle frequency $\omega/(2\pi)$ and stroke volume $2\pi Q_c/\omega$. Finally, the data acquisition system employs four pressure transducers (Basic ABP Series, Honeywell) and a DSB18B20 temperature probe with an Arduino Mega micro-controller interface for data collection. Data is stored onto a laptop using an open-source serial port reader and logger.

To ensure a controlled temperature and humidity, the apparatus, heat exchanger, reservoir, and sensors are positioned within an incubator (Fig. 3.6). The pump and the remaining components of the data acquisition system are situated outside the incubator. The pump drives fluid in a time-periodic manner through the device into a reservoir, with the outlet of the device exposed to the open atmosphere. The pump then draws fluid from the reservoir, repeating the cycle. This configuration allows for precise control and monitoring of the flow system while maintaining ideal cellular environmental conditions. In this connection, it is worth noting that successful experiments with live HUVECs and PAECs have been carried out using the MCS at biologically typical shear stresses and pressures over 24 hours. Details on these experiments are outside of the scope of this paper, which focuses instead on device design and flow dynamics.

3.3 Experimental Flow Diagnostics

Experimental flow diagnostics were conducted to evaluate the performance of the 3D-simplified model and device. To validate the theoretical model used in selecting the chamber aspect ratio, the flow streamlines were characterized experimentally and compared with the analytical predictions. In addition, measurements were taken to characterize the temporal pressure fluctuations

in the different chambers and ascertain whether the intra-chamber spatial pressure variations remain sufficiently small, as needed to guarantee that all cells within a given chamber are subject to nearly identical pulsating pressure forces. For completeness, the spatial pressure differences measured in the lab were compared with the theoretical prediction derived earlier, shown in Eq. (3.25). All of the flow diagnostics was performed with the fundamental frequency of the flow set to 1 Hertz (i.e. $\omega = 2\pi$ s^{-1}) and using water at 21 Celsius (i.e. $\mu/\rho \simeq 0.98 \times 10^{-6}$ m^2/s), giving a Womersley number $M \simeq 1.27$, as follows from evaluating Eq. (3.1) with $h = 0.6$ mm.

3.3.1 Particle Tracking Velocimetry

The fluid particle trajectories were measured using particle tracking velocimetry (PTV). To that end, beeswax pellets with a diameter smaller than 0.7 mm were introduced into the flow of the fabricated chamber. A high-speed monochrome camera, overlooking the top of the chamber, was used to capture video of the pellets traversing the chamber for 36 cycles of the pulsating flow. Subsequently, the individual frames were extracted and saved as grayscale images. These grayscale images were then processed using open source particle tracking software (Trackpy), that generated a data frame linking the positions of individual particles across different frames. This data frame was imported into MATLAB (MathWorks), where velocities in the x and y directions for each particle were computed at every frame using a first-order finite-difference scheme.

Data from 36 cycles were averaged within 24 15-degree bins to create an ensemble of a full cycle. Then for each frame of the cycle, the position and velocity information was sorted into a rectangular mesh spanning the flow domain. Outliers were filtered out by setting the lower and upper limits for velocity information in each box at the 2.5th and 97.5th quantiles, respectively. The average velocities within each computational cell were then evaluated per ensemble frame. Streamlines were derived from the average velocities through integration in the flow direction for each of the 24 frames of the ensemble. These phase-varying streamlines are depicted as cyan curves in Fig. 3.7. In addition, time-averaged streamlines were determined from the phase varying streamlines and superimposed in red. To enable comparisons with the theoretical predictions,

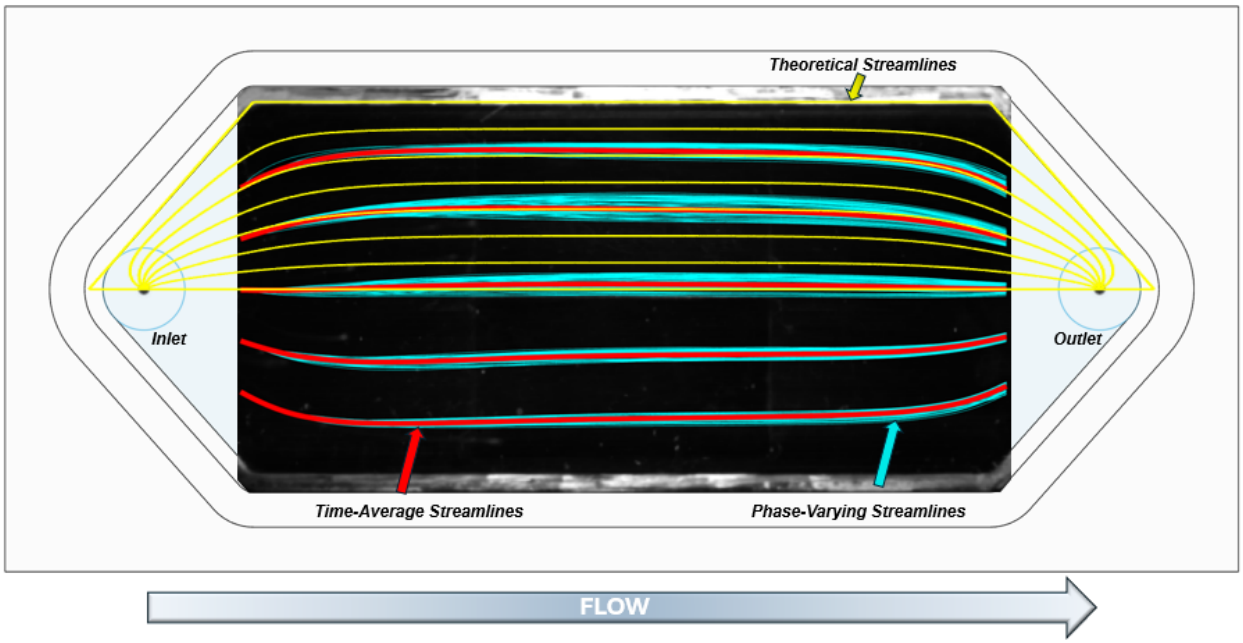

Figure 3.7: Comparison of phase-varying streamlines (cyan) and time-averaged streamlines (red) obtained using Particle Tracking Velocimetry with the theoretical predictions evaluated with use of $\psi(\hat{x}, \hat{y}) = \text{constant}$.

analytical streamlines (i.e. curves $\psi(\hat{x}, \hat{y}) = \text{constant}$) are represented as yellow curves.

The time-averaged streamlines (in red) and the theoretical streamlines (in yellow) shown in Fig. 3.7 closely coincide. Deviations are found near the inlet, where the time-averaged streamlines bow outward more than the theoretical streamlines. This can be attributed to the simplifications introduced in the theoretical model. Firstly, the analysis in the limit stated in Eq. (3.5) is strictly valid only in regions where the flow is fully developed, but not in the entrance region that extends over distances of order $\rho u_c h^2/\mu \ll W$ from the inlet, where the theoretical predictions are seen to depart from the experimental observations. In addition, in the theoretical description the inlet and outlet ports, with diameter D, are treated as singularities (i.e. a line source and a line sink) of infinitesimally small size, an approximation that involves errors of order D/W that likely contribute to the observed departures.

The comparisons in Fig. 3.7 also reveal that, while the theoretical streamlines are mirror symmetric about the center plane $\hat{x} = 0$, the experimental streamlines exhibit slight inward convergence, so that fluid particles tend to separate from the wall as they traverse the central part of the

chamber. This observation is consistent with the streamwise development of thin boundary layers on the external walls bounding laterally the chamber, an effect not accounted for in the theoretical description.

The theoretical framework posits that streamlines are independent of time, so that the phase-varying streamlines, represented by the cyan curves in Fig. 3.7, should overlap with the time-averaged streamlines. This overlap is apparent near the inlet, but becomes less evident on approaching the outlet. The observed departures are partly attributable to the influence of the lateral boundary layers, whose relative thickness oscillates during the cycle following the velocity fluctuations, and partly attributable to numerical error propagated during integration, which is initiated at the source, and also with the size and shape of particles, which hinder the accuracy of the particle tracking algorithm to identify and match particles effectively. Furthermore, the figure also displays differences between the phase-varying streamlines on the upper and lower halves of the image in Fig. 3.7 (cyan curves). These discrepancies are believed to be a result of nonuniformities in the spatial distribution of particles as well as small lateral asymmetries in flow near the inlet.

3.3.2 Oscillating Pressure Field

Pressure measurements were taken using the pressure ports located on the upper plate of the flow chambers. The measurements correspond to the idealized flow rate waveform depicted in Fig. 3.1 for a stroke volume of 8 mL (i.e. $Q_c = 8$ mL/s). Honeywell ABP transducers were utilized in this setup with data acquired using an Arduino Mega. Subsequently, the pressure data was imported into MATLAB (MathWorks). For the different measurements, an ensemble average was computed using 120 cycles, giving the results shown in Fig. 3.8.

The curves in Fig. 3.8a correspond to simultaneous readings using the downstream pressure ports of all four chambers. The pressure increases in all chambers during the first half of the cycle, during which there is significant flow, followed by a period of nearly zero pressure, coincident with the period of zero flow rate. The temporal pressure amplitude decays as we move downstream, with the pressure drop between subsequent chambers being related to the pressure loss along the

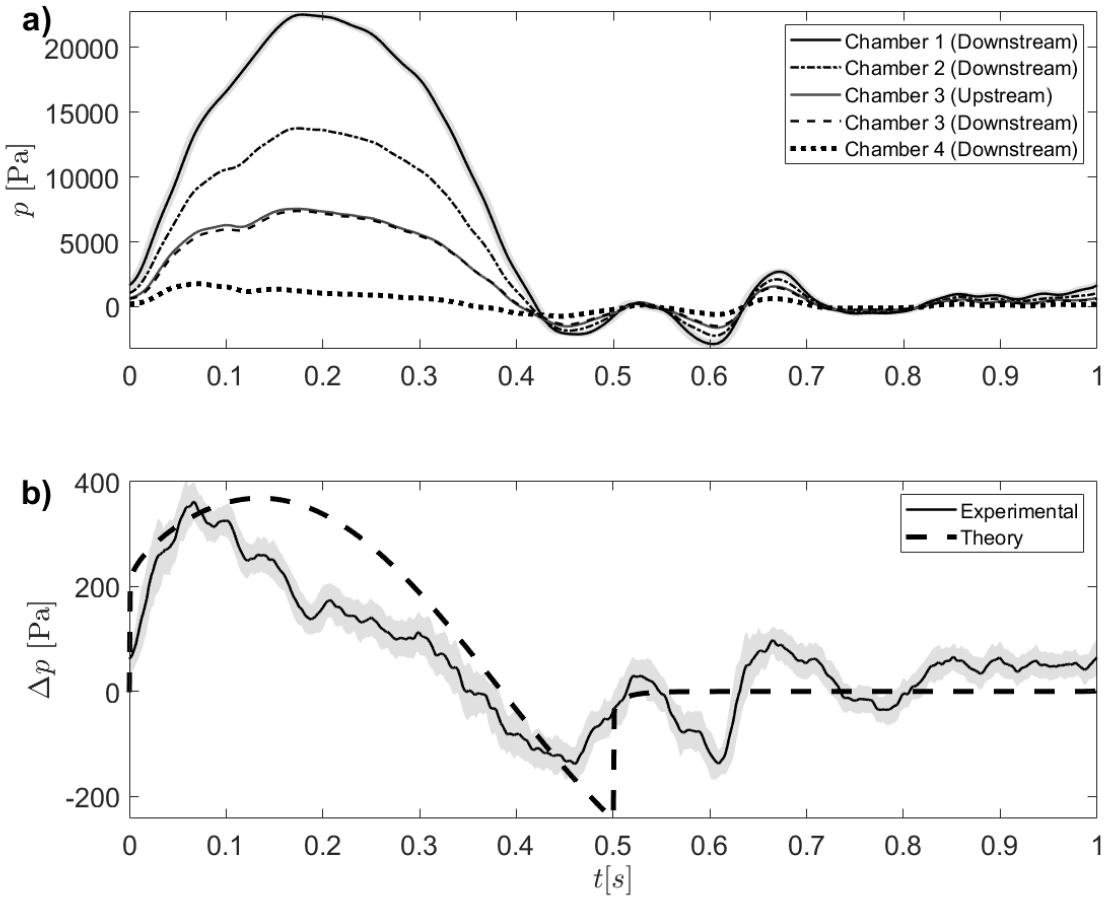

Figure 3.8: Experimental pressure measurements for the fabricated device using 120 cycles: (a) simultaneous pressure readings at the downstream pressure ports for the four chambers with the largest standard deviation (light gray) shown, alongside simultaneous pressure reading at the upstream port of the third chamber, and (b) instantaneous inter-port pressure difference in the third chamber with standard deviation (light gray) and theoretical predictions depicted.

connecting tubing. These pressure losses are to be compared with the much smaller pressure losses occurring within each chamber, which are characterized in Figs. 3.8b. Specifically, Fig. 3.8a shows the pressure found upstream and downstream of the testing region of the third chamber of the MCS, with their difference being represented in Fig. 3.8b.

An important observation from the plots in Fig. 3.8a is that the temporal pressure fluctuations measured at the two ports in the third chamber are nearly identical. Since the location of the two pressure ports, represented in Fig. 3.2c (see also the bottom plot of Fig. 3.5), are relatively far from

the edges of the testing region, it can be expected that the spatial pressure differences across the surface of the coverslip are even smaller than those between the two pressure ports, represented by the solid curve in Fig. 3.8b. Based on these considerations and on the quantitative information shown, one can expect that the departures in the pressure force experienced by different cells in a given coverslip will be on the order of 10%, an acceptable margin for experimental purposes.

The pressure difference between the two ports in the third chamber is compared in Fig. 3.8b with the theoretical prediction derived earlier. Spatial pressure measurements in other chambers give quantitatively similar results, in agreement with theoretical considerations. The nondimensional analytical result Eq. (3.25) is calculated using the dimensional form

$$\Delta p = \frac{\mu Q_c}{2h^3}\Delta\hat{p} \tag{3.29}$$

consistent with the scales introduced in section 3.1.2. As can be seen, the result predicts the waveform of the pressure difference reasonably well, including its general shape and peak amplitudes. However, as is clear from the comparison, the experimental measurements exhibit acoustic flow disturbances that appear as higher harmonics, not present in the acoustic-free prediction Eq. (3.25). These acoustic responses are likely associated with sharp pressure changes at the start and end of the pump cycle that can excite resonant disturbances in the system analogous to water hammer in pipes. The resulting pressure fluctuations are most apparent over the second part of the cycle (i.e. 0.5 s ¡ t < 1 s) where the primary pressure signal is small, but are also evident at the beginning of the cycle. These resonance effects, which are known to plague secondary measurement instruments, such as pressure sensors, were not accounted for when designing the flow system. Although a more careful design targeting a sufficiently high value of the system natural frequency combined with higher damping rates may have helped reduce acoustic effects [24, 25], for the specific waveform selected in our experiments, which induce significant harmonics associated with the sharp corners at the start and end of the wave, some level of acoustic fluctuations in the pressure signal is likely unavoidable. Fortunately, however, as can be concluded from the plots in Fig. 3.8, these acoustic

fluctuations remain much smaller than the temporal fluctuations of the fundamental frequency, so that their associated effects on the pressure force experienced by the cell can be expected to be relatively small.

3.4 Chapter Summary

To perform in vitro experiments involving pulmonary arterial cells, we engineered a biocompatible apparatus, the Multiplex Cell Shear (MCS). This device, comprising of four interconnected parallel plate chambers within a rigid framework, is designed to house a sizable cell population on coverslips. The MCS operates by subjecting cells to controlled and predominantly uniform shear stress at four distinct pressures ranges. In the design of the MCS, we have applied flow simplifications arising from the disparity of length and time scales present in the problem to derive a reduced model describing pulsatile flow through parallel-plate chambers of arbitrary planform. This theoretical model allows for separation of the spatial and temporal components of the solution, thereby facilitating the analysis of the fluid dynamics for any planform shape, Womersley number, and flow-rate inputs.

The temporal component of the flow, contingent upon flow rate profiles and Womersley number, was evaluated for both a simplified and a desired flow rate profile, with results given in Figs. 3.3 and 3.4, respectively. We specifically considered the temporal response of wall shear stress, pressure gradients, and velocities for increasing values of the Womersley number. The spatial structure of the flow was characterized by computing streamlines and accompanying spatial distributions of wall shear stress for a hexagonal planform of varying aspect ratio Λ. It was seen that for values of Λ exceeding $\Lambda = 2.9$ the spatial variations of wall shear stress in the testing region remain below 2%, a value that was deemed to be sufficiently small for cell-testing purposes.

A comprehensive flow system featuring four parallel-plate chambers with $\Lambda = 2.9$ connected in series was designed, built and tested using different experimental diagnostics. The streamlines measured using particle tracking velocimetry were found to be in good agreement with theoretical

predictions. Accompanying measurements of temporal and spatial pressure variations demonstrated that the pressure forces experienced in a given testing region are nearly uniform, and that fluctuations introduced by acoustic effects, although nonnegligible, remain relatively small. The results from these experimental flow diagnostics therefore indicate that the device meets all the design goals necessary for the in-vitro experiments that inspired its creation.

3.5 Acknowledgment

Chapter 3, in full, is a reprint of the material as it appears in Campos, O. A., Garcia-Herreros, A., Sánchez, A. L., Fineman, J. R., & Pawlak, G. (2024). A Multichamber Pulsating-Flow Device With Optimized Spatial Shear Stress and Pressure for Endothelial Cell Testing. *Journal of Biomechanical Engineering*, *147*.The dissertation author was the primary investigator and author of this paper.

Bibliography

[1] Massaaki S, Toshiro O. Biorheological views of endothelial cell responses to mechanical stimuli. Biorheology. 2005;.

[2] Jufri NF, Mohamedali A, Avolio A, Baker MS. Mechanical stretch: physiological and pathological implications for human vascular endothelial cells. Vasc Cell. 2015;7.

[3] Lim XR, F HO. Mechanosensing-by-vascular-endothelium. Annu Rev Physiol. 2024;86:71–97.

[4] Johnson Kameny R, Datar SA, Boehme JB, Morris C, Zhu T, Goudy BD, et al. Ovine models of congenital heart disease and the consequences of hemodynamic alterations for pulmonary artery remodeling. Am J Respir Cell Mol Biol. 2019;60:503–514.

[5] Fallon ME, Mathews R, Hinds MT. In Vitro Flow Chamber Design for the Study of Endothelial Cell (Patho)Physiology. J Biomech Eng. 2022 Feb;144.

[6] Meng F, Cheng H, Qian J, Dai X, Huang Y, Fan Y. In vitro fluidic systems: Applying shear stress on endothelial cells. Med Nov Technol Devices. 2022;15:100143.

[7] Batchelor GK. An introduction to fluid dynamics. Cambridge University Press; 1967.

[8] Félétou M. The Endothelium: Part 1: Multiple Functions of the Endothelial Cells—Focus on Endothelium-Derived Vasoactive Mediators. Morgan & Claypool Life Sciences Publishers; 2011.

[9] Krüger-Genge A, Blocki A, Franke R P F and Jung. Vascular Endothelial Cell Biology: An Update. Int J Mol Sci. 2019;.

[10] Voyvodic PL, Min D, Baker AB. A multichannel dampened flow system for studies on shear stress-mediated mechanotransduction. Lab on a Chip. 2012;12(18):3322–3330.

[11] Loudon C, Tordesillas A. The Use of the Dimensionless Womersley Number to Characterize the Unsteady Nature of Internal Flow. J Theor Biol. 1998 Mar;191:63–78.

[12] Yakhot A, Arad M, Ben-Dor G. Numerical investigation of a laminar pulsating flow in a rectangular duct. Int J Numer Methods Fluids. 1999 Apr;29:935–950.

[13] Bacabac RG, Smit TH, Cowin SC, Van Loon JJWA, Nieuwstadt FTM, Heethaar R, et al. Dynamic shear stress in parallel-plate flow chambers. J Biomech. 2005 Jan;38:159–167.

[14] Avari H, Rogers KA, Savory E. Wall Shear Stress Determination in a Small-Scale Parallel Plate Flow Chamber Using Laser Doppler Velocimetry Under Laminar, Pulsatile and Low-

Reynolds Number Turbulent Flows. J Fluids Eng. 2018 Jun;140.

[15] Blythman R, Persoons T, Jeffers N, Nolan KP, Murray DB. Localised dynamics of laminar pulsatile flow in a rectangular channel. Int J Heat and Fluid Flow. 2017;66:8–17.

[16] Frangos JA, McIntire LV, Eskin SG. Shear stress induced stimulation of mammalian cell metabolism. Biotechnol Bioeng. 1988 Oct;32:1053–1060.

[17] van Kooten TG, Schakenraad JM, Van Der Mei HC, Busscher HJ. Development and use of a parallel-plate flow chamber for studying cellular adhesion to solid surfaces. J Biomed Mater Res A. 1992;26:725–738.

[18] Ruel J, Lemay J, Dumas G, Doillon C, Charara J. Development of a Parallel Plate Flow Chamber for Studying Cell Behaviour Under Pulsatile Flow. ASAIO J. 1995;29:876–883.

[19] Nauman EA, Risic KJ, Keaveny TM, Satcher RL. Quantitative Assessment of Steady and Pulsatile Flow Fields in a Parallel Plate Flow Chamber. Ann Biomed Eng. 1999 Mar;27:194–199.

[20] Chung BJ, Robertson AM, Peters DG. The numerical design of a parallel plate flow chamber for investigation of endothelial cell response to shear stress. Comput Struct. 2003 May;81:535–546.

[21] Lane WO, Jantzen AE, Carlon TA, Jamiolkowski RM, Grenet JE, Ley MM, et al. Parallel-plate Flow Chamber and Continuous Flow Circuit to Evaluate Endothelial Progenitor Cells under Laminar Flow Shear Stress. J Vis Exp. 2012 Jan;p. 3349.

[22] Qin K, Hu X, Liu Z. Analysis of Pulsatile Flow in the Parallel-Plate Flow Chamber with Spatial Shear Stress Gradient. J Hydrodyn. 2007 Feb;19:113–120.

[23] Cheng CP, Herfkens RJ, Taylor CA, Feinstein A J. Proximal Pulmonary Artery Blood Flow Characteristics in Healthy Subject Measured in an Upright Posture Using MRI: The Effects of Exercise and Age. J Magn Reson Imaging. 2005;21:752–758.

[24] Walton TEF, Ireland KC. Principles of pressure transducer function and sources of error in clinical use. Anaesth Intensive Care Med. 2020;21:668–672.

[25] Back M, Carroll C. Principles of pressure transducers, resonance, damping and frequency response. Anaesth Intensive Care Med. 2023;24:720–724.

Chapter 4

Poiseuille Flow with a Stretching Bottom Wall

4.1 Introduction

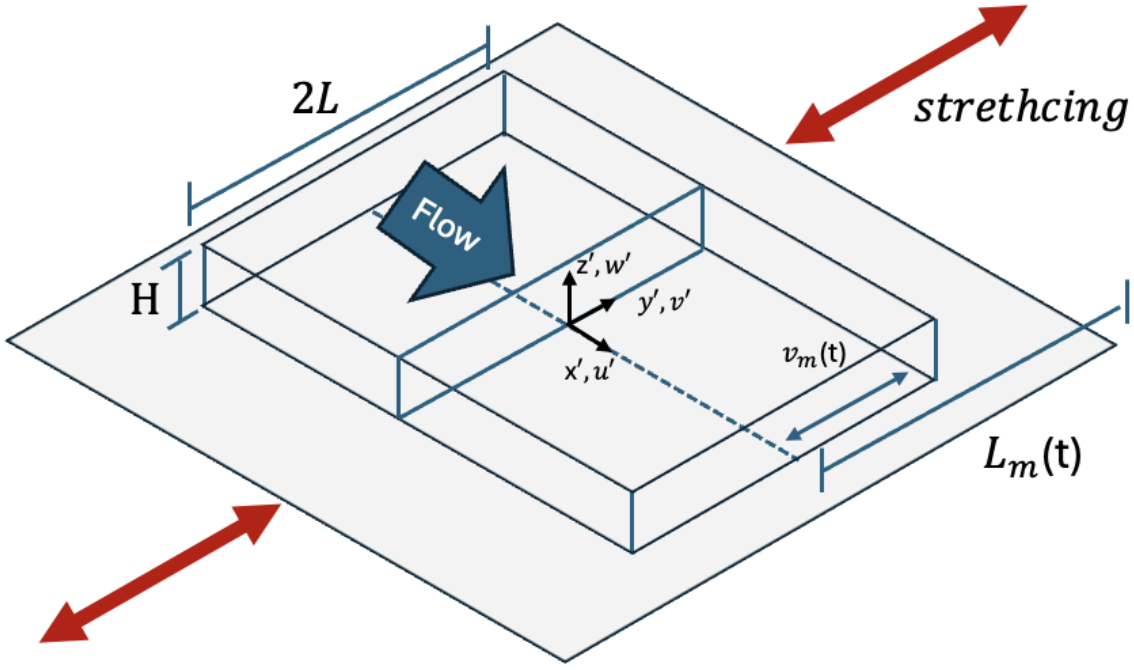

Figure 4.1: Theoretical schematic of flow entering a Hele-Shaw cell with a stretching bottom.

Children with congenital heart disease are at risk of developing pulmonary vascular remodeling and pulmonary hypertension, conditions that increase right ventricular load and can ultimately reduce life expectancy [1, 2]. The interior of the vascular network is lined by endothelial cells, which are responsible for maintaining healthy arteries and veins. Because endothelial cells play a central role in sensing and responding to the local hemodynamic environment, understanding how pulmonary endothelial cells respond to mechanical loading is an important step toward clarifying

disease progression and identifying possible therapeutic strategies [3–6]. *In vivo*, these cells are exposed not to a single isolated force, but to a coupled mechanical environment that includes fluid shear stress, transmural pressure, and circumferential stretch [3–5]. Reproducing these conditions *in vitro* is therefore essential for studying endothelial mechanobiology in a controlled and physiologically meaningful way [7, 8].

For studies aimed at downstream analyses such as RNA sequencing, an experimental platform to achieve this controlled mechanical environment must also accommodate sufficiently large cell populations while maintaining precise and reproducible control of the applied loads. In previous work, our group developed and characterized a multi-chamber pulsating-flow device that enables large endothelial cell samples to be exposed to uniform pulsatile shear stress while experiencing different pressure ranges across chambers [9]. The present work extends that effort by focusing on the theoretical and experimental analysis of Poiseuille flow with a stretchable bottom wall with hopes that this work can be used to create a device in the future capable of imposing coupled loading conditions relevant to vascular and pulmonary endothelial cells. More broadly, this effort reflects the continuing shift in mechanobiology from simplified single-input systems toward *in vitro* devices that more closely reconstruct the coupled mechanical environment experienced by cells *in vivo* [7, 8, 10].

Historically, devices developed for endothelial mechanobiology have tended to study shear stress and stretch separately. Shear stress studies have commonly employed parallel plate or Hele-Shaw type flow chambers because these systems allow well characterized wall shear stress to be generated over adherent cell monolayers under laminar flow conditions [11–17]. These chambers have been widely adopted because of their geometric simplicity, optical accessibility, and the relative ease with which shear stress can be estimated from chamber geometry, fluid properties, and volumetric flow rate [11, 12, 14]. Over time, these systems have been extended beyond steady flow to include pulsatile and oscillatory forcing, although many studies still analyze such flows under quasi-steady assumptions or focus primarily on steady-flow operation [14, 15, 18–20].

In parallel, numerous stretching platforms have been developed to study the effect of

substrate deformation on adherent cells. These include uniaxial, biaxial, and equiaxial membrane-based systems, as well as more complex three-dimensional constructs [7, 21, 22]. Among these, planar membrane-based stretching devices remain especially prominent because they permit direct imaging, well-controlled loading, and straightforward integration into cell culture workflows [21, 22]. However, despite the large body of work on shear stress and stretch applied independently, these approaches do not fully reproduce the coupled loading environment experienced by endothelial cells in vivo [5, 7, 10].

To address this limitation, several groups have developed devices that apply shear stress and stretch simultaneously. Some of the earliest combined-loading systems relied on compliant tubing or vessel-like geometries, in which fluid flow generated both wall shear stress and circumferential deformation [23, 24]. While these systems improved physiological realism, they generally did not permit independent control of the two stimuli and were often less convenient for direct visualization and mechanistic study [24]. More recent microfluidic and membrane-based devices have enabled shear stress and cyclic stretch to be applied either independently or simultaneously, thereby allowing more systematic investigation of coupled endothelial responses [10, 24]. Nevertheless, many of these systems remain focused on steady-flow conditions, or otherwise do not directly address how pulsatile flow interacts with a dynamically deforming wall [8, 14, 18].

This limitation is important because pulsatility is a defining feature of physiological cardiovascular flow. In parallel-plate systems, unsteady flow behavior depends on channel geometry, forcing frequency, and viscous diffusion timescales, and under some conditions the wall shear stress can no longer be treated as quasi-steady [14, 18, 25–27]. As a result, when wall motion is added to an already unsteady flow field, theoretical analysis becomes necessary to determine how the moving boundary modifies the fluid motion and the mechanical environment seen by the cells.

In the present study, we develop an experimental facility that uses a Hele-Shaw-type flow chamber with a stretchable bottom boundary. Our primary objective is to characterize the effect of this coupled system under Poiseuille flow. To do so, we combine theoretical analysis with experimental flow visualization, allowing the influence of the moving bottom wall on the fluid

motion to be assessed directly. This combined framework provides a basis for future development of device that can apply all hemodynamic loads onto endothelial cells accurately with conditions associated with pulmonary vascular disease.

4.2 Unsteady Viscous Flow in a Cell Shearer with a Stretching Bottom

4.2.1 The model problem

An infinitely long rectangular channel, represented by the section in Fig. 4.1, has a height H and semi-width $L \gg H$. The channel contains a fluid of density ρ and kinematic viscosity ν whose motion is to be described using Cartesian coordinates (x', y', z') and corresponding velocity components (u', v', w'). The fluid moves axially under the action of a time-periodic longitudinal pressure gradient

$$-\frac{1}{\rho}\frac{\partial p'}{\partial x'} = A_o \Pi(\omega t'), \tag{4.1}$$

with characteristic value A_o and dimensionless waveform $\Pi(\omega t')$, where t' represents the time and ω is the angular frequency. The bottom wall is covered with an elastic membrane of width $2L_m$ that is stretched symmetrically in the transverse direction as described by

$$L_m/L_o = 1 + \varepsilon S(\omega t'), \tag{4.2}$$

where L_o is a reference length, ε is the stretching ratio and $S(\omega t')$ is an order-unity time-periodic function. The associated velocity on the surface of the membrane v'_m, linearly proportional to the distance y' from the symmetry axis, can be computed according to

$$v'_m = \frac{y'}{L_m}\frac{\mathrm{d}L_m}{\mathrm{d}t'} = \varepsilon\omega y' \frac{\dot{S}}{1 + \varepsilon S}, \tag{4.3}$$

where $\dot{S}$ represents the derivative of the stretching function S with respect to its argument $\omega t'$.

Since the channel is infinitely long, the velocity components $u'(y', z', t')$, $v'(y', z', t')$, and $w'(y', z', t')$ of the resulting periodic flow are independent of x'. The motion in the cross-sectional plane is independent of the longitudinal motion, but the latter is coupled to the former through the transverse convective terms. This one-way coupled solution is compatible with a pressure field of the form $p'/\rho = \tilde{p}'(y', z', t') - A_o x' \Pi(\omega t')$.

The solution can be simplified for cross sections with large aspect ratio $L/H \gg 1$, when the flow in the central part of the channel (i.e. at distances $L - |y| \gg H$) is slender, with velocities $v' \sim \varepsilon\omega L \gg w' \sim \varepsilon\omega H$. This slender flow is flanked by short turn-around regions located near the lateral boundary walls, at distances $L - |y| \sim H$, where $v' \sim w' \sim \varepsilon\omega L$. Since the region containing the endothelial cells is typically positioned in the central portion of the device, we restrict our attention on this region sufficiently far from the side walls and do not consider the lateral near-wall regions.

The analysis is restricted to channels with large aspect ratio, $L/H \gg 1$, and small stretching ratio, $\varepsilon \ll 1$. The characteristic oscillation time, ω^{-1}, is assumed to be comparable to the viscous diffusion time across the channel height, H^2/ν. This corresponds to an order-unity Womersley number,

$$\alpha = \left(\frac{\omega H^2}{\nu}\right)^{1/2} \sim 1, \tag{4.4}$$

which is the regime of primary interest in endothelial-cell experiments.

4.2.2 Flow in the central region

Nondimensional formulation

The flow in the central region is described using the appropriately scaled order-unity dimensionless variables $t = \omega t'$, $y = y'/L$, $z = z'/H$, $u = u'/(A_o H^2/\nu)$, $v = v'/(\varepsilon\omega L)$, $w =$

$w'/(\varepsilon\omega H)$, and $\tilde{p} = \tilde{p}'/(\varepsilon\omega L^2\nu/H^2)$. The transverse motion is determined by integration of

$$\frac{\partial v}{\partial y} + \frac{\partial w}{\partial z} = 0 \tag{4.5}$$

$$\alpha^2\left[\frac{\partial v}{\partial t} + \varepsilon\left(v\frac{\partial v}{\partial y} + w\frac{\partial v}{\partial z}\right)\right] = -\frac{\partial \tilde{p}}{\partial y} + \left(\frac{H}{L}\right)^2\frac{\partial^2 v}{\partial y^2} + \frac{\partial^2 v}{\partial z^2} \tag{4.6}$$

$$\alpha^2\left[\frac{\partial w}{\partial t} + \varepsilon\left(v\frac{\partial w}{\partial y} + w\frac{\partial w}{\partial z}\right)\right] = -\left(\frac{H}{L}\right)^{-2}\frac{\partial \tilde{p}}{\partial z} + \left(\frac{H}{L}\right)^2\frac{\partial^2 w}{\partial y^2} + \frac{\partial^2 w}{\partial z^2} \tag{4.7}$$

with boundary conditions

$$v - \frac{y\dot{S}}{1+\varepsilon S} = w = 0 \text{ at } z = 0 \quad \text{and} \quad v = w = 0 \text{ at } z = 1, \tag{4.8}$$

while the longitudinal motion is determined by integration of

$$\alpha^2\left[\frac{\partial u}{\partial t} + \varepsilon\left(v\frac{\partial u}{\partial y} + w\frac{\partial u}{\partial z}\right)\right] = \Pi + \left(\frac{H}{L}\right)^2\frac{\partial^2 u}{\partial y^2} + \frac{\partial^2 u}{\partial z^2} \tag{4.9}$$

with boundary conditions

$$u = 0 \text{ at } z = 0, 1. \tag{4.10}$$

The above problem is to be solved in the double limit $\varepsilon \ll 1$ and $H/L \ll 1$. Although the analysis can be performed for general 2π-periodic functions $S(t)$ and $\Pi(t)$, results are presented below for channels with sinusoidally-stretched membranes ($S = \sin t$) subject to a constant longitudinal pressure gradient $\Pi = 1$. In this case, the longitudinal velocity reduces at leading order for $\varepsilon \ll 1$ to the familiar Poiseuille expression

$$u = \frac{1}{2}z(1-z), \tag{4.11}$$

while the motion in the transverse plane can be described by introducing asymptotic expansions of the form

$$v = v_0 + \varepsilon v_1 + \cdots, \quad w = w_0 + \varepsilon w_1 + \cdots, \quad \tilde{p} = \tilde{p}_0 + \varepsilon\tilde{p}_1 + \cdots. \tag{4.12}$$

At the first two orders in the expansion, the solution will be seen to be independent of the channel aspect ratio provided that

$$(H/L)^2 \ll \varepsilon, \tag{4.13}$$

that being the case considered here.

Transverse motion

The transverse motion in the cross-sectional plane can be determined independently of the longitudinal motion. Substituting (4.12) into (4.5)–(4.8) and collecting terms of order unity yields, at leading order, the reduced equations

$$\frac{\partial v_0}{\partial y} + \frac{\partial w_0}{\partial z} = 0, \quad \alpha^2 \frac{\partial v_0}{\partial t} = -\frac{\partial \tilde{p}_0}{\partial y} + \frac{\partial^2 v_0}{\partial z^2}, \quad \frac{\partial \tilde{p}_0}{\partial z} = 0 \tag{4.14}$$

with no-slip conditions

$$v_0 - y\cos t = w_0 = 0 \text{ at } z = 0 \quad \text{and} \quad v_0 = w_0 = 0 \text{ at } z = 1. \tag{4.15}$$

The problem can be solved in terms of a reduced stream function $f_0(z)$ defined such that

$$v_0 = y\,\mathrm{Re}\left(f_{0z}\mathrm{e}^{\mathrm{i}t}\right) \quad \text{and} \quad w_0 = -\,\mathrm{Re}\left(f_0\mathrm{e}^{\mathrm{i}t}\right), \tag{4.16}$$

where the subscript z denotes differentiation with respect to the vertical coordinate. The complex function $f_0(z)$ is determined by integrating the boundary-value problem

$$f_{0zzzz} - \mathrm{i}\alpha^2 f_{0zz} = 0; \quad f_0(0) = f_{0z}(0) - 1 = f_0(1) = f_{0z}(1) = 0, \tag{4.17}$$

to yield

$$f_0 = C_1 + C_2 z + C_3\mathrm{e}^{\Lambda z} + C_4\mathrm{e}^{-\Lambda z}, \tag{4.18}$$

where $\Lambda = \alpha(1+\mathrm{i})/\sqrt{2}$ and

$$\begin{aligned}\frac{\Lambda C_1}{\mathrm{e}^{\Lambda}(\Lambda-1)+\mathrm{e}^{-\Lambda}(\Lambda+1)} &= \frac{C_2}{2-\mathrm{e}^{\Lambda}-\mathrm{e}^{-\Lambda}} \\ &= \frac{-\Lambda C_3}{\mathrm{e}^{-\Lambda}(\Lambda+1)-1} \\ &= \frac{-\Lambda C_4}{\mathrm{e}^{\Lambda}(\Lambda-1)+1} \\ &= \frac{1}{\mathrm{e}^{\Lambda}(\Lambda-2)-\mathrm{e}^{-\Lambda}(\Lambda+2)+4}.\end{aligned} \tag{4.19}$$

The first order corrections to the leading order solution, obtained by collecting terms of order ϵ, are described in Appendix 4A.

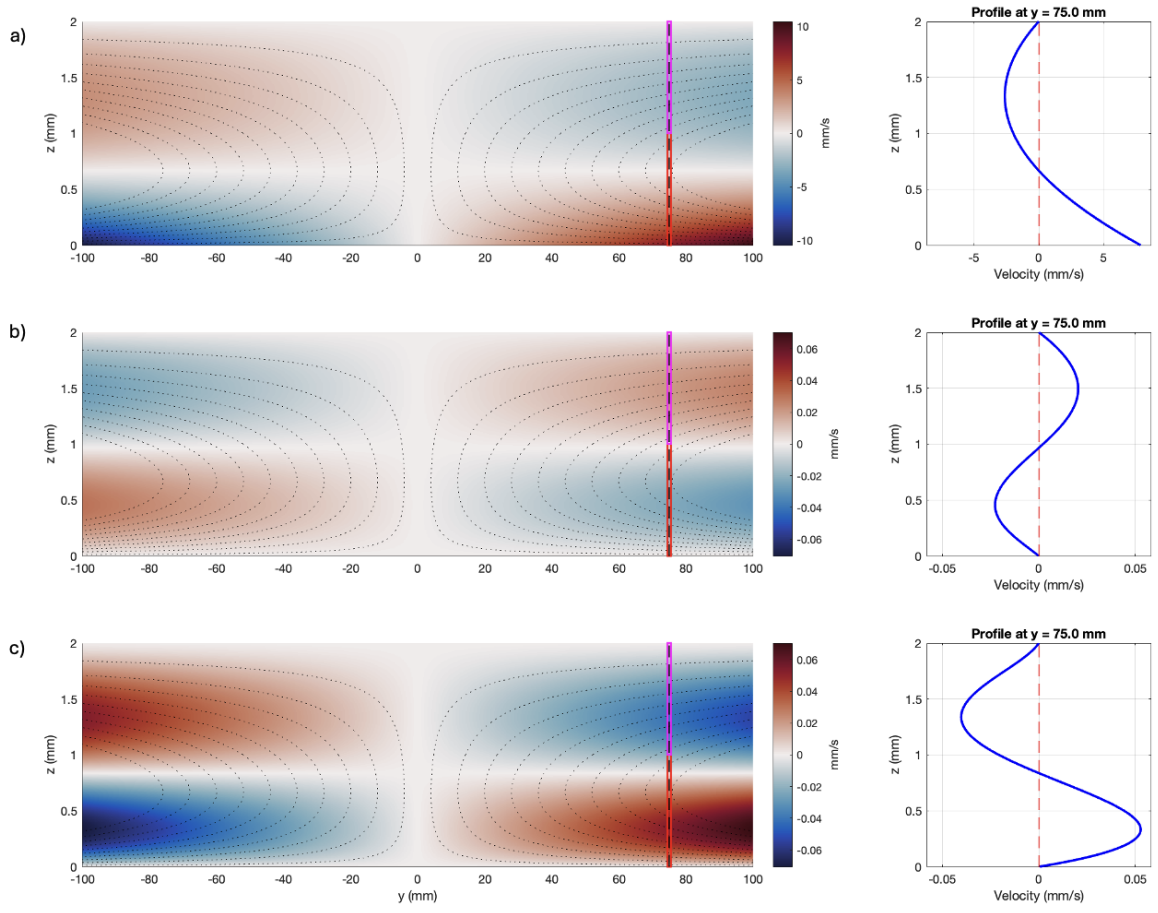

Figure 4.2: Theoretical transverse-flow predictions: (a) leading-order solution, (b) steady correction, and (c) unsteady correction, with vertical velocity profiles, at 75 mm, shown on the right column for each prediction.

The transverse velocity cross section are detailed in Fig. 3.4. For both the leading order solution and its corrections, the streamlines follow a consistent pattern, originating from the lateral walls and converging near the center. The solution exhibits symmetry, reflected across the center of the chamber. Because the system utilizes sinusoidal wall motion, the maximum and minimum velocities are temporal mirrors of one another. Observations of the leading-order and unsteady corrections show that transverse motion is most intense at the bottom of the chamber and weakens toward the top. Velocity profiles at a location corresponding to the experimental measurement location, 75 mm, are also shown in the right column.

4.3 Experiment Setup

4.3.1 Setup

Experiments were conducted within a rectangular tank measuring 718 mm in length, 300 mm in width, and 63.5 mm in height. Inside this tank, a custom flow chamber featuring a stretchable floor was constructed from two primarily assembled components. The first, lower assembly (shown in blue in Fig. 4.3a) acts as the foundation. It consists of a 6.35 mm-thick base plate that spans the entire tank floor, featuring precisely machined slots. These slots allow for the accurate positioning of two large transverse false walls, each 12.7 mm thick. Located 194 mm from either end of the tank, these false walls effectively partition the main volume into three distinct regions: an intake reservoir, a main central reservoir, and an outtake reservoir. Within the main reservoir, two lateral walls (shown in yellow in Fig. 4.3b and c), each 12.7 mm thick and 2 mm high, are spaced 100 mm apart to channel the fluid flow. To ensure structural stability, flat bars extending from the top of the false walls to the tub's sides allow this entire lower assembly to be securely bolted into place.

The second, upper assembly (shown in red in Fig. 4.3a) defines the ceiling of the flow chamber and houses an upper viewing window. Its core is a rigid 12.7 mm thick base plate that serves directly as the top wall of the flow chamber, surrounded by outer walls that create the viewing area. This upper component is bolted directly to the flat bars of the lower assembly. Its lateral

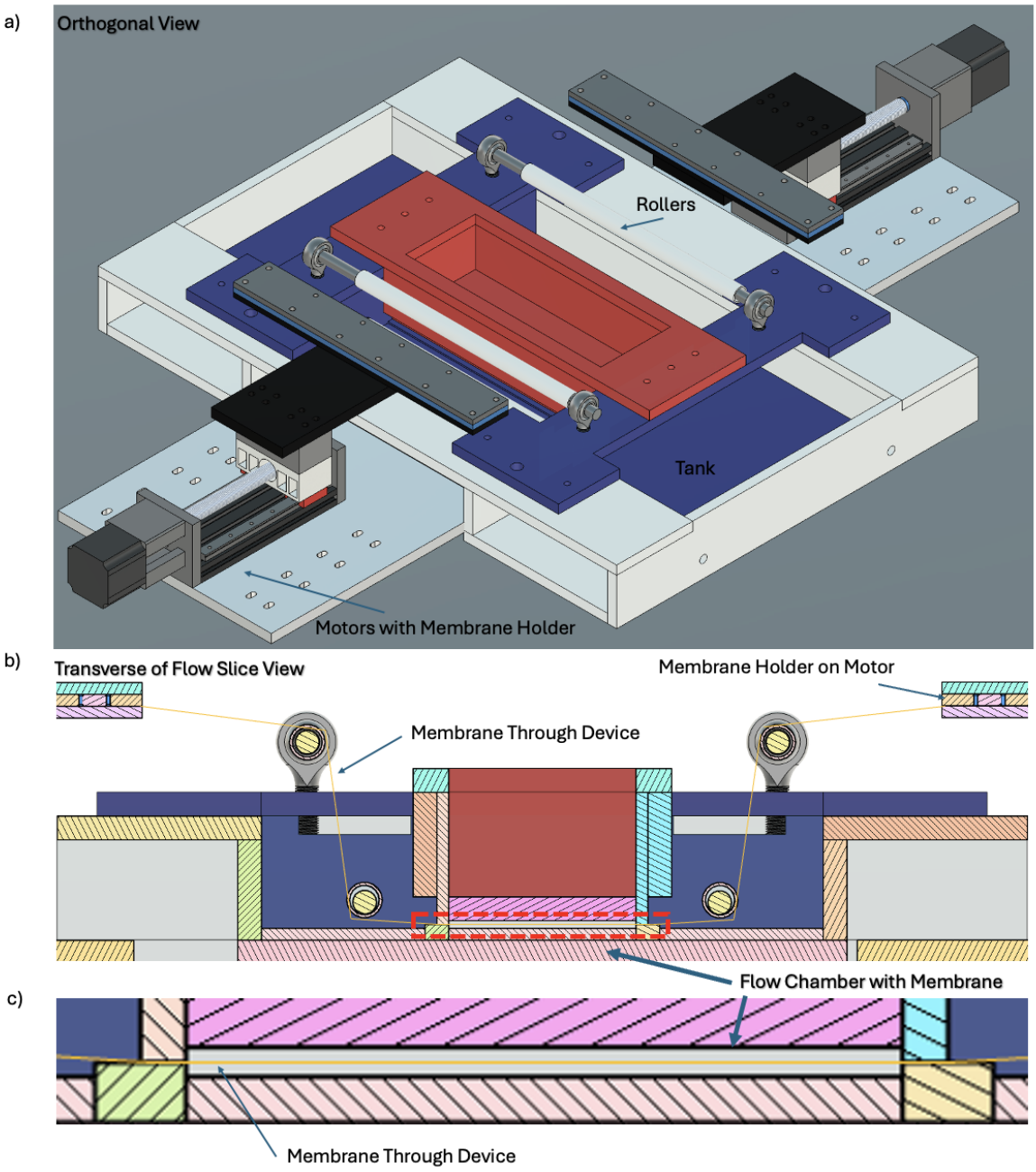

Figure 4.3: CAD-generated views of the experimental setup, including the stretching mechanism, membrane holder, and flow chamber assembly.

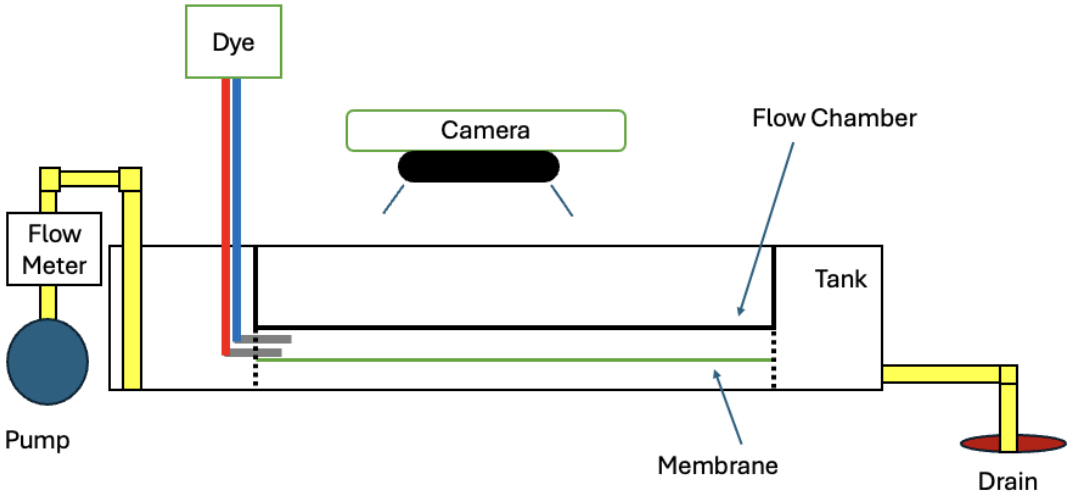

Figure 4.4: Flow schematic of the experimental setup showing the tank, flow chamber, membrane, camera, and dye injection arrangement.

walls (shown in Fig. 4.3b and c), which are 6.35 mm thick, extend 2 mm below the base plate to strictly define the vertical clearance of the flow chamber. Because of this configuration, the upper assembly hovers exactly 0.2 mm above the lower lateral walls. This 0.2 mm gap allows a stretchable membrane to be threaded between the two assemblies, effectively acting as the dynamic bottom wall of the flow chamber.

During operation, the system relies on precise mechanical and fluid control. The membrane is secured to two external motors using a specialized clamping mechanism (labeled 'membrane clamp' in Fig. 4.3a), which ensures the membrane material remains perfectly smooth and free of wrinkles during deformation. These motors are able to stretch the membrane bidirectionally in a continuous, sinusoidal pattern at a prescribed frequency of 1 Hz. For the experiments discussed here, only one motor was used, stretching the membrane from one side. While the floor of the chamber is actively stretching, fluid is driven through the channel by a pressure gradient. This gradient is established by creating a difference in fluid height, achieved by operating a pump. To maintain a controlled environment and prevent any recirculating dye from contaminating the flow field, the system utilizes an open-loop system, as seen in Fig. 4.4: one pump constantly draws fresh water that is sent to the tank, with an inline flow meter used to verify the flow rate, while fluid is

discharged from the tank via a drainage.

Deriving Specific Theoretical Results

With our experimental observations (described in the next section) confined to a viewing window positioned at the top of the flow chamber, we are only able to capture horizontal motion. Consequently, our analysis focuses primarily on derived theoretical solutions for the lateral flow. The theoretical streamlines are plotted along with the lateral flow velocity in Fig. 4.2. Within these visualizations, blue (upper) and red (lower) bounding boxes indicate the specific locations where the dye injection needles are located. We extract an average of the localized velocities from this region to be our estimate. Because we consider unidirectional stretching, we use twice the experimental chamber width in the theoretical estimates.

4.3.2 Longitudinal Flow Measurement

To assess the steady longitudinal flow in the chamber, the motion of dye was tracked using video. Using MATLAB, the trajectory of the dye was tracked across multiple frames and the measured displacement over time is then used to calculate the average velocity of the fluid in the chamber. This experimental value was then cross-validated against the theoretical average velocity, which was calculated based on the input flow rate recorded by an inline flow meter.

4.3.3 Transverse Flow Visualization and Measurement

The transverse flow was visualized and measured using a dual-needle injection mechanism to create distinct streaklines within the chamber. Two needles, each 1 mm in diameter, are stacked vertically within the flow field. The upper needle discharges blue dye, while the lower needle discharges red dye. To ensure precise vertical stratification, the densities of the dyes are carefully controlled. The blue dye is diluted with water to match the density of the surrounding fluid, preventing it from sinking. Conversely, the red dye is injected at its undiluted, higher concentration; this increased density intentionally allows the red dye to settle and remain closer to the bottom wall

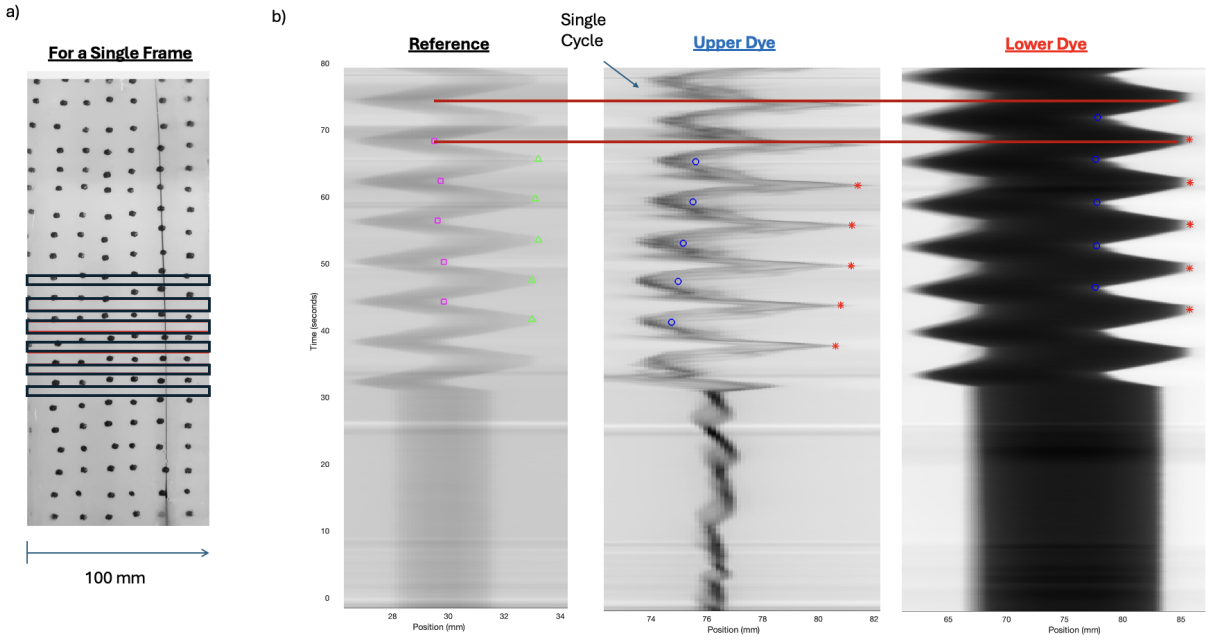

Figure 4.5: (a) Flow region analyzed for the blue dye motion and (b) time-stack images of the upper and lower dye traces.

of the flow chamber.

To simplify the experimental parameters and isolate specific flow behaviors, the membrane is stretched uni-directionally rather than bidirectionally. The left edge of the membrane is mechanically fixed in place, effectively creating a stationary boundary, while a single motor drives the actuation from the opposite side.

With the dye flowing slowly from an open reservoir, the system is first brought to a steady-state flow, allowing the fluid to circulate until any initial transient disturbances have completely decayed. Once steady flow is confirmed, the single motor is activated to introduce the uni-directional stretching of the bottom membrane. The membrane undergoes this continuous stretching for approximately 15 cycles. After the 15th cycle, the motor is halted, and the flow is monitored as it returns to its initial steady-state condition As illustrated in Fig. 4.4, an overhead camera continuously captures the evolution of the injected lines over the full sequence through the transparent viewing port located in the upper (red) assembled component.

To measure the motion of the membrane, a sequence of images is collected without dye.

For each image, a longitudinal section of each video image spanning a set of dots is averaged. The averaged row from each image is assembled to produce a time-stack showing lateral distance versus time (e.g. Fig. 4.5b) where the membrane motion appears as a sinusoidal path. A set of lateral positions and corresponding times are digitized manually for the lateral extrema in each image. The amplitude and phase of the periodic stretching is then determined from these data.

To assess the lateral motion of the dye lines, sets of rows that provide a clear view of the dye are selected and averaged (Fig. 4.5a). Rows from each of the images are assembled to produce a time-stack as for the membrane motion, showing lateral distance vs time (Fig. 4.4b). Amplitude and relative phase of the dye motion can then be calculated in a similar fashion to the membrane motion with an uncertainty based on the standard deviation in measurements.

By comparing the respective maximum and minimum positions between the reference data and the dyes, we calculated the phase shift angle of the flow. For each dye, these extrema were utilized to determine the distance traveled within the imaging frame. Then a backward and forward velocity was found using the extrema derived distances and dividing them by half cycle. These velocities were then averaged between all cycles.

4.4 Results

Flow Analysis and Velocity Characterization

Experiments were carried out with an inlet flow rate of 0.8 LPM. Given that the channel is partitioned by a membrane into two sections, a primary section of interest with a height of 2 mm and a secondary section with a height of 3 mm,we estimate the flow rate entering the visualization chamber to be 0.3 LPM. Based on the chamber dimensions (2 mm height by 100 mm width), the theoretical vertically averaged velocity using eq 4.11 is 25.24 mm/s. However, experimental flow visualization using dye tracking yielded a measured average velocity of 13.33 mm/s. For all subsequent analyses, this measured value of 13.33 mm/s is utilized as the baseline average velocity.

Theoretical Traverse Velocity Dynamics

As the experiments here focus on unidirectional stretching, we examine the half solution, specifically focusing on the regions of the blue (upper) and red (lower) dashed boxes in Fig. 4.2, which correspond to the dye injection locations. The mean transverse velocities are summarized in Table 4.1.

Table 4.1: Mean transverse velocities for the analyzed dye regions, derived for the maximum velocities. The bottom and top regions correspond to the red and blue dye-tracking regions, respectively.

Max/Min Velocity	**Upper**	**Lower**
Leading-order	−1.96 mm/s	1.97 mm/s
Steady correction	0.01 mm/s	–0.01 mm/s
Unsteady correction	−0.03 mm/s	0.03 mm/s

Qualitative Flow Visualization Results

The experimental results for the upper and lower dye tracers are as follows:

Table 4.2: Experimental velocity and phase shift measurements for upper and lower dye tracers.

Parameter	**Upper Dye**	**Lower Dye**
Max/Min Velocity	1.98 ± 0.05 mm/s	2.68 ± 0.02 mm/s
Phase Shift	193.82° ± 5.28°	5.15° ± 4.58°

The phase shifts were calculated relative to the reference. The phase shift are close to 180 degree shift for upper dye and close to 0 for lower dye, as seen with a single cycle in Fig. 4.5b.

4.5 Discussion

The experimental results in Fig. 4.2 and Table 4.1 show that the leading-order solution captures the dominant behavior of the transverse flow, while the higher-order corrections provide

only minor modifications and Table 4.1 show that the leading-order solution captures the dominant behavior of the transverse flow, while the higher-order corrections provide only minor modifications.

The discrepancy between the flow rate measurement via dye tracking and the theoretically predicted value is likely associated with separate flow paths that route fluid around the experimental channel. For instance, the rollers, false walls, and membrane create potential avenues where fluid can be diverted. For this reason, the velocity values obtained from dye tracking are considered to provide a more representative measurement of the local flow within the experimental chamber.

Now focusing on dye measurements, the upper dye measurements show good agreement with values estimated by integrating the theoretical solution over the upper half of the solution. The lower dye measurements, however, show larger discrepancies relative to the estimates for the lower half of the solution, as seen in Table 4.2. The difference here is likely due to uncertainty in the vertical location of the lower dye. The complex experimental setup limited visualization to a top-down view so the vertical location of the dye could not be measured directly.

As noted earlier, the undiluted dye used for the lower injection was slightly denser than the working fluid which resulted in some downward flow and spreading, as evident in Fig. 4.5. The vertical average over the needle location, illustrated in Fig. 4.5 thus will give an overestimate of the velocity. Assuming that the dye is limited to a region closer to the bottom of the channel yields a lateral velocity of 8 mm/s, indicating that the dye is closer to the estimated injection location.

4.6 Chapter Summary

This chapter developed and characterized a Hele-Shaw-type flow chamber with a stretchable bottom boundary to better understand how membrane stretching affects flow in a pressure-driven chamber. The work combined theoretical predictions with dye-based flow visualization to examine the flow before and during membrane actuation. The theory indicates that the longitudinal flow remains steady, governed by Poiseuille solution. The first-order corrections from membrane stretching are small and do not significantly modify the streamwise velocity.

The dye-visualization results show good general agreement with the theoretical solution. In the absence of membrane stretching, dye streaklines remain steady. With the introduction of a stretching lower boundary, the dye shows a sinusoidal lateral motion. Dye in the lower region is in phase with the membrane while the upper tracer is shifted by roughly 180 degrees. The upper dye measurements agree reasonably well with the predicted transverse velocities. The lower dye measurements show larger deviations, likely because the actual vertical position of the lower dye was uncertain. Overall, the results show that membrane stretching primarily drives transverse oscillatory motion as predicted by the theoretical solution. These findings provide a useful starting point for improving the chamber design and for developing a cell-shearing device that can apply both flow-induced shear and substrate stretching to endothelial cells.

Appendix 4A: Derivation of First Order Corrections

The first-order corrections are obtained by collecting terms of order ε in (4.5)–(4.8). If terms of order $(H/L)^2$ are neglected, consistent with the assumption (4.13), then the problem reduces to the integration of

$$\begin{gathered}\frac{\partial v_1}{\partial y}+\frac{\partial w_1}{\partial z}=0,\\ \alpha^2\left[\frac{\partial v_1}{\partial t}+v_0\frac{\partial v_0}{\partial y}+w_0\frac{\partial v_0}{\partial z}\right]=-\frac{\partial \tilde{p}_1}{\partial y}+\frac{\partial^2 v_1}{\partial z^2},\\ \frac{\partial \tilde{p}_1}{\partial z}=0.\end{gathered} \tag{4.20}$$

with boundary conditions

$$v_1+\frac{y}{2}\sin(2t)=w_1=0 \text{ at } z=0 \quad \text{and} \quad v_1=w_1=0 \text{ at } z=1. \tag{4.21}$$

Using the identity

$$\mathrm{Re}(A\mathrm{e}^{\mathrm{i}t})\,\mathrm{Re}(B\mathrm{e}^{\mathrm{i}t})=\frac{1}{2}\mathrm{Re}(AB^*)+\frac{1}{2}\mathrm{Re}(AB\mathrm{e}^{2\mathrm{i}t}), \tag{4.22}$$

where A and B are time-independent complex functions and the asterisk denotes complex conjugates, allows us to write the convective terms in the compact form

$$v_0\frac{\partial v_0}{\partial y}+w_0\frac{\partial v_0}{\partial z}=\frac{y}{2}\,\mathrm{Re}\left[\left(f_{0z}f_{0z}^*-f_0f_{0zz}^*\right)+\left(f_{0z}^2-f_0f_{0zz}\right)\mathrm{e}^{2\mathrm{i}t}\right]. \tag{4.23}$$

The form of this equation suggests that the velocity correction (v_1, w_1) consists of a steady component (v_1^s, w_1^s) and an unsteady, time-periodic component (v_1^u, w_1^u) with twice the frequency of the stretching motion. Owing to the linearity of the problem defined in (4.20)–(4.21), these components can be determined independently, as demonstrated below.

The steady component, corresponding to the streaming flow generated by the stretching

membrane, satisfies the problem

$$\frac{\partial v_1^s}{\partial y} + \frac{\partial w_1^s}{\partial z} = 0, \quad \alpha^2 y \mathcal{H}^s = -\frac{\mathrm{d}\tilde{p}_1^s}{\mathrm{d}y} + \frac{\partial^2 v_1^s}{\partial z^2}; \quad v_1 = w_1 = 0 \text{ at } z = 0, 1, \tag{4.24}$$

where

$$\mathcal{H}^s(z) = \frac{1}{2}\,\mathrm{Re}\left(f_{0z} f_{0z}^* - f_0 f_{0zz}^*\right). \tag{4.25}$$

Using in (4.24) the ansatz

$$v_1^s = y\alpha^2 f_{1z}^s \quad \text{and} \quad w_1^s = -\alpha^2 f_1^s, \tag{4.26}$$

involving the reduced streamfunction $f_1^s(z)$, yields

$$f_{1zzzz}^s = \mathcal{H}_z^s, \quad f_1^s(0) = f_{1z}^s(0) = f_1^s(1) = f_{1z}^s(1) = 0, \tag{4.27}$$

which can be integrated to give

$$\begin{aligned} f_1^s = &-\frac{z^2}{2}\int_0^1 (1-z)(1-3z)\mathcal{H}^s \mathrm{d}z - z^3 \int_0^1 z(1-z)\mathcal{H}^s \mathrm{d}z \\ &+ \frac{1}{2}\int_0^z \bar{z}^2\,\mathcal{H}^s \mathrm{d}\bar{z} - z\int_0^z \bar{z}\,\mathcal{H}^s \mathrm{d}\bar{z} + \frac{z^2}{2}\int_0^z \mathcal{H}^s \mathrm{d}\bar{z}, \end{aligned} \tag{4.28}$$

where $\bar{z}$ represents a dummy integration variable.

Similarly, the unsteady component of the velocity corrections can be expressed in the form $v_1^u = y\alpha^2\,\mathrm{Re}\left(f_{1z}^u \mathrm{e}^{2\mathrm{i}t}\right)$ and $w_1^u = -\alpha^2\,\mathrm{Re}\left(f_1^u \mathrm{e}^{2\mathrm{i}t}\right)$, where the complex stream function $f_1^u(z)$ satisfies

$$f_{1zzzz}^u - 2\mathrm{i}\alpha^2 f_{1zz}^u = \mathcal{H}_z^u, \quad f_1^u(0) = f_{1z}^u(0) - \frac{\mathrm{i}}{2} = f_1^u(1) = f_{1z}^u(1) = 0, \tag{4.29}$$

with

$$\mathcal{H}^u(z) = \frac{1}{2}\left(f_{0z}^2 - f_0 f_{0zz}\right). \tag{4.30}$$

Integrating (4.29) yields

$$\begin{aligned} f_1^u(z) = {} & D_1 + D_2 z + D_3 e^{\mu z} + D_4 e^{-\mu z} \\ & + \left[-\frac{1}{2}\frac{C_3(C_2 - \Lambda C_1)}{\Lambda^2} + \frac{1}{2}\frac{C_2 C_3}{\Lambda} z \right] e^{\Lambda z} \\ & + \left[-\frac{1}{2}\frac{C_4(C_2 + \Lambda C_1)}{\Lambda^2} - \frac{1}{2}\frac{C_2 C_4}{\Lambda} z \right] e^{-\Lambda z}, \qquad \mu^2 = 2\Lambda^2. \end{aligned} \tag{4.31}$$

which completes the determination of the velocity correction

$$v_1 = y\alpha^2 \left[f_{1z}^s + \mathrm{Re}\left(f_{1z}^u \mathrm{e}^{2\mathrm{i}t} \right) \right] \quad \text{and} \quad w_1 = -\alpha^2 \left[f_1^s + \mathrm{Re}\left(f_1^u \mathrm{e}^{2\mathrm{i}t} \right) \right]. \tag{4.32}$$

The undetermined coefficients,D_n, can be numerically solved using boundary conditions.

Bibliography

[1] Johnson Kameny R, Datar SA, Boehme JB, Morris C, Zhu T, Goudy BD, et al. Ovine models of congenital heart disease and the consequences of hemodynamic alterations for pulmonary artery remodeling. Am J Respir Cell Mol Biol. 2019;60:503–514.

[2] Cheng CP, Herfkens RJ, Taylor CA, Feinstein JA. Proximal Pulmonary Artery Blood Flow Characteristics in Healthy Subject Measured in an Upright Posture Using MRI: The Effects of Exercise and Age. J Magn Reson Imaging. 2005;21:752–758.

[3] Krüger-Genge A, Blocki A, Franke RP, Jung F. Vascular Endothelial Cell Biology: An Update. Int J Mol Sci. 2019;20(18):4411.

[4] Félétou M. The Endothelium: Part 1: Multiple Functions of the Endothelial Cells—Focus on Endothelium-Derived Vasoactive Mediators. Morgan & Claypool Life Sciences Publishers; 2011.

[5] Lim XR, Harraz OF. Mechanosensing by vascular endothelium. Annu Rev Physiol. 2024;86:71–97.

[6] Sato M, Ohshima N. Biorheological views of endothelial cell responses to mechanical stimuli. Biorheology. 2005;.

[7] Brown TD. Techniques for mechanical stimulation of cells in vitro: A review. J Biomech. 2000;33(1):3–14.

[8] Davis CA, Zambrano S, Anumolu P, Allen ACB, Sonoqui L, Moreno MR. Device-Based In Vitro Techniques for Mechanical Stimulation of Vascular Cells: A Review. J Biomech Eng. 2015;137(4):040801.

[9] Campos OA, Garcia-Herreros A, Sánchez AL, Fineman JR, Pawlak G. A Multichamber Pulsating-Flow Device With Optimized Spatial Shear Stress and Pressure for Endothelial Cell Testing. J Biomech Eng. 2025;147(1):011006.

[10] Davis C, Zambrano-Roman B, Sridhar R, Jastram A, Chakraborty S, Zawieja D, et al. A bioreactor for in vitro studies of lymphatic endothelial cells with simultaneous fluid shear stress and membrane strain. J Mech Behav Biomed Mater. 2025;164:106909.

[11] Meng F, Cheng H, Qian J, Dai X, Huang Y, Fan Y. In vitro fluidic systems: Applying shear stress on endothelial cells. Med Nov Technol Devices. 2022;15:100143.

[12] Fallon ME, Mathews R, Hinds MT. In Vitro Flow Chamber Design for the Study of Endothelial Cell (Patho)Physiology. J Biomech Eng. 2022;144.

[13] van Kooten TG, Schakenraad JM, Van Der Mei HC, Busscher HJ. Development and use of a parallel-plate flow chamber for studying cellular adhesion to solid surfaces. J Biomed Mater Res. 1992;26:725–738.

[14] Bacabac RG, Smit TH, Cowin SC, Van Loon JJWA, Nieuwstadt FTM, Heethaar R, et al. Dynamic shear stress in parallel-plate flow chambers. J Biomech. 2005;38:159–167.

[15] Nauman EA, Risic KJ, Keaveny TM, Satcher RL. Quantitative Assessment of Steady and Pulsatile Flow Fields in a Parallel Plate Flow Chamber. Ann Biomed Eng. 1999;27:194–199.

[16] Chung BJ, Robertson AM, Peters DG. The numerical design of a parallel plate flow chamber for investigation of endothelial cell response to shear stress. Comput Struct. 2003;81:535–546.

[17] Lane WO, Jantzen AE, Carlon TA, Jamiolkowski RM, Grenet JE, Ley MM, et al. Parallel-plate Flow Chamber and Continuous Flow Circuit to Evaluate Endothelial Progenitor Cells under Laminar Flow Shear Stress. J Vis Exp. 2012;p. 3349.

[18] Qin K, Hu X, Liu Z. Analysis of Pulsatile Flow in the Parallel-Plate Flow Chamber with Spatial Shear Stress Gradient. J Hydrodyn. 2007;19:113–120.

[19] Avari H, Rogers KA, Savory E. Wall Shear Stress Determination in a Small-Scale Parallel Plate Flow Chamber Using Laser Doppler Velocimetry Under Laminar, Pulsatile and Low-Reynolds Number Turbulent Flows. J Fluids Eng. 2018;140.

[20] Ruel J, Lemay J, Dumas G, Doillon C, Charara J. Development of a Parallel Plate Flow Chamber for Studying Cell Behaviour Under Pulsatile Flow. ASAIO J. 1995;29:876–883.

[21] Jufri NF, Mohamedali A, Avolio A, Baker MS. Mechanical stretch: physiological and pathological implications for human vascular endothelial cells. Vasc Cell. 2015;7.

[22] Zhao J, Meng F, Qian J, Huang Y, Fan Y. In vitro cell stretching devices and their applications: From cardiomyogenic differentiation to tissue engineering. Med Nov Technol Devices. 2023;18:100220.

[23] Moore JE, Burki E, Suciu A. A device for subjecting vascular endothelial cells to both fluid shear stress and circumferential cyclic stretch. Ann Biomed Eng. 1994;22:416–422.

[24] Zheng W, Jiang B, Wang D, Zhang W, Wang Z, Jiang X. A microfluidic flow-stretch chip for investigating blood vessel biomechanics. Lab on a Chip. 2012;12:3441–3450.

[25] Loudon C, Tordesillas A. The Use of the Dimensionless Womersley Number to Characterize the Unsteady Nature of Internal Flow. J Theor Biol. 1998;191:63–78.

[26] Blythman R, Persoons T, Jeffers N, Nolan KP, Murray DB. Localised dynamics of laminar pulsatile flow in a rectangular channel. Int J Heat Fluid Flow. 2017;66:8–17.

[27] Yakhot A, Arad M, Ben-Dor G. Numerical investigation of a laminar pulsating flow in a rectangular duct. Int J Numer Methods Fluids. 1999;29:935–950.

Chapter 5

Conclusion

This dissertation examined physiologically relevant flows through a combination of theoretical modeling, experimental measurement, and engineering design. Although the systems considered in the preceding chapters are distinct, but they have a common objective to use fluid mechanics to better understand, measure, and reproduce flow phenomena that are important in biomedical settings. Taken together, the chapters presented here demonstrate how fluid mechanics can be applied both to the quantification of slow flow processes in physiological systems and to the development of experimental platforms that recreate disease relevant flow environments.

Chapter 2 focused on cerebrospinal fluid motion in an idealized spinal-canal geometry and evaluated the capability of Time-SLIP MRI to resolve the small cycle-to-cycle displacements associated with mean Lagrangian transport. Because these net displacements are small relative to the dominant oscillatory motion, their measurement presents a significant challenge. By combining phantom design, MRI measurements, image processing, and simulation-based comparisons, this chapter assessed both the promise and the limitations of Time-SLIP MRI as a noninvasive tool for detecting weak transport phenomena. The results showed that the method can provide useful information regarding cumulative displacement trends under controlled conditions, while also making clear that measurement fidelity is strongly influenced by factors such as signal quality, spatial resolution, and post-processing methodology.

Chapter 3 addressed a complementary problem, the generation and characterization of physiologically relevant flow environments for endothelial-cell studies motivated by pulmonary hypertension. In that chapter, a framework was developed for a multiplex cell-shearing apparatus capable of exposing cells to combinations of pulsatile flow, pressure variation, and wall

induced mechanical loading. The analysis combined theory, numerical modeling, and experiment to characterize the resulting flow, pressure, and shear-stress environments across multiple chambers connected in series. This work established the governing principles needed to interpret and control the mechanical conditions generated within the device.

Chapter 4 extends in a related direction by examining Poiseuille flow in a Hele-Shaw-type chamber with a stretchable bottom wall. The chapter combined analytical development with dye-based flow visualization to determine how membrane stretching modifies the chamber flow. The results showed that the primary effect of stretching is the production of transverse oscillatory motion that can be measured. In this way, the chapter complements Chapter 3 by isolating and clarifying the role of wall motion in a simplified but physically relevant configuration, while also opening future framework needed to develop a device that applies all three mechanical loads accurately onto endothelial cells.

Several opportunities remain for future work. In the context of cerebrospinal-fluid transport, further studies are needed to extend the present measurements beyond idealized geometries and to evaluate how imaging-based transport estimates compare with more physiologically detailed models and experiments. In the context of endothelial mechanobiology, additional work is needed to refine the operating conditions of the multiplex flow system and to connect the characterized mechanical environment with specific biological responses. For the stretching-bottom chamber, future studies should first develop an apparatus based on the analysis conducted. For the stretching boundary experiments, future studies should first develop an apparatus that incorporates a stretching boundary building on the analysis conducted. An effective design will need to address design challenges including incorporating direct cellular experiments in a contained sterile device. More broadly, future investigations should continue to integrate theoretical analysis, numerical simulation, and experimental validation to improve both the measurement of physiological flows and the design of systems that reproduce them.